

Chapter 1

Recent Advances (2012–2015) in the Photocatalytic Conversion of Carbon Dioxide to Fuels Using Solar Energy: Feasibility for a New Energy

Yasuo Izumi*

Department of Chemistry, Graduate School of Science, Chiba University,
Yayoi 1-33, Inage-ku, Chiba 263-8522, Japan

*E-mail: yizumi@faculty.chiba-u.jp

In this chapter, recent advances in photocatalytic CO₂ conversion with water and/or other reductants are reviewed for the publications between 2012 and 2015. Quantitative comparisons were made for the reaction rates in $\mu\text{mol h}^{-1} \text{g}_{\text{cat}}^{-1}$ to ascertain the progress of this field although the rates depends on photocatalyst conditions and reaction conditions (temperature, pressure, and photon wavelength and flux). TiO₂ photoproduced methane or CO from CO₂ and water at rates of 0.1–17 $\mu\text{mol h}^{-1} \text{g}_{\text{cat}}^{-1}$ depending on the crystalline phase, crystalline face, and the defects. By depositing as minimal thin TiO₂ film, the rates increased to 50–240 $\mu\text{mol h}^{-1} \text{g}_{\text{cat}}^{-1}$. Gaseous water was preferred rather than liquid water for methane/CO formation as compared to water photoreduction to H₂. Pt, Pd, Au, Rh, Ag, Ni, Cu, Au₃Cu alloy, I, MgO, RuO₂, graphene, g-C₃N₄, Cu-containing dyes, and Cu-containing metal-organic frameworks (MOFs) were effective to assist the CO₂ photoreduction using TiO₂ to methane (or CO, methanol, ethane) at rates of 1.4–160 $\mu\text{mol h}^{-1} \text{g}_{\text{cat}}^{-1}$. Metals of greater work function were preferred. By depositing as minimal thin photocatalyst film, the rates increased to 32–2200 $\mu\text{mol h}^{-1} \text{g}_{\text{cat}}^{-1}$. The importance of crystal face of TiO₂ nanofiber was suggested. As for semiconductors other than TiO₂, ZnO, Zn₆Ti layered double hydroxide (LDH), Mg₃In LDH, KTaO₃, In(OH)₃, graphene, graphene oxide, g-C₃N₄, CoTe, ZnO,

ZnTe, SrTiO₃, ZnGa₂O₄, Zn₂GeO₄, Zr–Co–Ir oxides, Nb₂O₅, HNbO₃, NaNbO₃, InNbO₄, NiO, Co₃O₄, Cu₂O, AgBr, carbon nanotube, and the composites of these were reported to form methane, CO, methanol, acetaldehyde from CO₂ and water at rates of 0.15–300 μmol h⁻¹ g_{cat}⁻¹ that were comparable to rates using promoted TiO₂. The band energy designs comprising appropriate conduction band for CO₂ reduction and valence band for water oxidation were made progresses in these semiconductors and semiconductor junctions in the three years. If H₂ was used as a reductant, Ni/SiO₂-Al₂O₃ formed methane at 423 K under pressurized CO₂ + H₂ at a rate of 55 mmol h⁻¹ g_{cat}⁻¹. This rate was not enabled by heating the system under dark, suggesting photoactivated reaction followed by thermally-assisted reaction(s) via Ni–H species. As pure photocatalytic reactions from CO₂ + H₂, methanol formation rates were improved up to 0.30 μmol h⁻¹ g_{cat}⁻¹ by the doping of Ag/Au nanoparticles, [Cu(OH)₄]²⁻ anions, and Cu-containing dyes to Zn–Ga LDH. Furthermore, sacrificial reductants, e.g. hydrazine, Na₂SO₃, methanol, triethanol amine, and triethylamine, were also utilized to form CO, formate, and methanol at rates of 20–2400 μmol h⁻¹ g_{cat}⁻¹ using semiconductor or MOF photocatalysts. Finally, similar to the integrated system of semiconductor photocatalyst for water oxidation and metal complex/enzyme catalyst for CO₂ (photo)reduction, two semiconductors (WO₃, Zn–Cu–Ga LDH) were combined on both side of proton-conducting polymer to form methanol at a rate of 0.05 μmol h⁻¹ g_{cat}⁻¹ from CO₂ and moisture. These promotion of photoconversion rates of CO₂ and new photocatalysts found in these three years have indicated the way beyond for a new energy.

Introduction

To enable carbon neutral cycle in modern industrial society, CO₂ conversion into fuels utilizing natural (sustainable) energy is one of the ideal methods. Carbon monoxide, methane, methanol, acetaldehyde, and ethane obtained from CO₂ are attractive products because they can be easily intergrated into the existing fuel and chemical technology. Although various review articles have been published dealing with the conversion of solar energy into fuels (1, 2) and the conversion of CO₂ into fuels (3–8) until 2012, the researches and developments are more intensive during 2012 and 2015 for the target of CO₂ reduction into fuels that enables carbon neutral and suppresses the anthropogenic increase of CO₂ concentrations in the atmosphere.

In this chapter, recent advance based on various intensive researches between 2012 and 2015 in the CO₂ photoconversion into fuels is reviewed in hope for a new energy. Similar to previous review for studies before early 2012 (4), the scope

of this chapter is limited to semiconductor photocatalysis for the conversion of CO₂. Especially, some orders of increase for the CO₂ conversion rates and new photocatalysts are focused.

Photon Energy Conversion of CO₂ to Fuels with Water

1. TiO₂ Photocatalysts

1.1. Difference of Crystal Phases

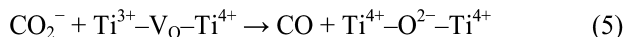
The CH₄ formation rate was 0.19 μmol h⁻¹ g_{cat}⁻¹ in atmospheric pressure of CO₂ and moisture using TiO₂ (9). Under similar reaction conditions using some crystal phases of TiO₂, the CO formation rates were in the order

$$\text{anatase (3.3 } \mu\text{mol h}^{-1} \text{ g}_{\text{cat}}^{-1}\text{)} > \text{brookite (1.5 } \mu\text{mol h}^{-1} \text{ g}_{\text{cat}}^{-1}\text{)} > \text{rutile (0.82 } \mu\text{mol h}^{-1} \text{ g}_{\text{cat}}^{-1}\text{)} \text{ (Table 1).}^{10} \quad (1)$$

If the TiO₂ photocatalysts were preheated at 483 K in a flow of helium to make defects, the CO formation rates were in the order

$$\text{brookite (17 } \mu\text{mol h}^{-1} \text{ g}_{\text{cat}}^{-1}\text{)} > \text{anatase (10 } \mu\text{mol h}^{-1} \text{ g}_{\text{cat}}^{-1}\text{)} > \text{rutile (4.0 } \mu\text{mol h}^{-1} \text{ g}_{\text{cat}}^{-1}\text{)} \quad (2).$$

The order did not change if minor methane formation was added to the CO formation (Table 1). The binding of CO₂ on Ti³⁺ sites and the reduction of the bound CO₂⁻ species by O-defect sites were suggested (10).



The activity order reported in reference (11) was consistent with equation 1. Furthermore, the anatase:brookite phase ratio was varied by changing the amount of urea used during the TiO₂ synthesis. The improved photoconversion of CO₂ suggested heterojunction effects of two crystalline phases.

$$\text{anatase (75\%)-brookite (25\%)} > \text{P25 (anatase 80\%, rutile 20\%)} > \text{anatase} > \text{brookite} \quad (6)^{11}$$

Table 1. Reported CO₂ Photoreduction Catalysts, Reaction Conditions, and the Formation Rates in Water/with Moisture Using TiO₂

<i>Photocatalyst</i>		<i>Reactants</i>		<i>T (K)</i>	<i>Light source</i>	<i>Reactor</i>	<i>Major product {formation rate ($\mu\text{mol h}^{-1} \text{g}_{\text{cat}}^{-1}$)}</i>	<i>Ref</i>
<i>Brand name</i>	<i>Amount (mg)</i>	<i>CO₂</i>	<i>H₂O</i>					
P25	10	Atmosph. P	Atmosph. P	Room T	100W Hg	Closed	CH ₄ (0.19)	(9)
TiO ₂ (anatase)	100	99 kPa	2.3 kPa		150 W solar simulator	Stainless steel, Flow	CO (3.3)	(10)
TiO ₂ (rutile)							CO (0.82)	(10)
TiO ₂ (brookite)							CO (1.5)	(10)
Defective TiO ₂ (anatase) ^a							CO (10.4), CH ₄ (2.5)	(10)
Defective TiO ₂ (rutile) ^a							CO (4.0)	(10)
Defective TiO ₂ (brookite) ^a							CO (17.0), CH ₄ (1.9)	(10)
TiO ₂ (anatase)	100	Atmosph. P	Saturated		150 W solar simulator	Stainless steel	CO (1.2)	(11)
TiO ₂ (anatase:brookite =3:1)							CO (2.1)	(11)
TiO ₂ (brookite)							CO (0.7)	(11)
TiO ₂ (anatase) {010}	100	101 kPa	Liq (1 mL)	293	300 W Hg	Pyrex	CH ₄ (1.2)	(12)

<i>Photocatalyst</i>		<i>Reactants</i>		<i>T (K)</i>	<i>Light source</i>	<i>Reactor</i>	<i>Major product {formation rate ($\mu\text{mol h}^{-1} \text{g}_{\text{cat}}^{-1}$)}</i>	<i>Ref</i>
<i>Brand name</i>	<i>Amount (mg)</i>	<i>CO₂</i>	<i>H₂O</i>					
TiO ₂ (anatase) {101}							CH ₄ (0.74)	(12)
TiO ₂ (anatase) {001}							CH ₄ (0.19)	(12)
TiO ₂ (anatase) {001}:{101} =11:89	100						CH ₄ (0.15)	(13)
TiO ₂ (anatase) {001}:{101} =58:42							CH ₄ (1.4)	(13)
TiO ₂ (anatase){001}: {101}=83:17							CH ₄ (0.55)	(13)
P25	20	200 kPa	12.3 kPa	323	100 W Xe	Stainless steel	CO (1.2), CH ₄ (0.38)	(15)
P25	20	200 kPa	Liq (4 mL)	323	100 W Xe	Stainless steel	CO (0.80), CH ₄ (0.11)	(15)
TiO ₂ (anatase)	500	Saturated	Liq (1 L)	303	UV lamp	Pyrex	CH ₄ (11)	(18)
TiO ₂ nanofiber	5	Atmosph. <i>P</i>	Satur. <i>P</i>		500 W Xe		CO (12), CH ₄ (6)	(20)
TiO ₂ (anatase)	Film	Atmosph. <i>P</i>	Satur. <i>P</i>	Room <i>T</i>	400 W Xe	Stainless steel, Flow	CO (240)	(26)

Continued on next page.

Table 1. (Continued). Reported CO₂ Photoreduction Catalysts, Reaction Conditions, and the Formation Rates in Water/with Moisture Using TiO₂

<i>Photocatalyst</i>		<i>Reactants</i>		<i>T (K)</i>	<i>Light source</i>	<i>Reactor</i>	<i>Major product {formation rate ($\mu\text{mol h}^{-1} \text{g}_{\text{cat}}^{-1}$)}</i>	<i>Ref</i>
<i>Brand name</i>	<i>Amount (mg)</i>	<i>CO₂</i>	<i>H₂O</i>					
P25	1.25 cm ² Film	190 kPa	Satur. <i>P</i>	<333	1000W Xe	Aluminum	CH ₄ (50)	(27)
TiO ₂	100						CH ₄ (0.52)	(29)

^a Heated at 493 K for 90 min in a flow of He.

1.2. Difference of Crystal Facets

The reactivity order for facets in the CO₂ photoreduction to methane using anatase TiO₂ was reported

$$\{0\ 1\ 0\} > \{1\ 0\ 1\} > \{0\ 0\ 1\} \quad (7) \text{ (Table 1).}^{12}$$

The ratio of exposed $\{0\ 0\ 1\}$ face versus thermodynamically stable $\{1\ 0\ 1\}$ face was progressively varied between 11:89 and 83:17 for anatase TiO₂ utilizing the F⁻ as stabilizing agent for the $\{0\ 0\ 1\}$ face (13). The conduction band (CB) and valence band (VB) for $\{0\ 0\ 1\}$ face were calculated to position at slightly negative energy, thereby photoexcited electrons and holes move to $\{1\ 0\ 1\}$ and $\{0\ 0\ 1\}$ faces, respectively, similar to normal heterojunction of two kinds of semiconductors (Figure 1). The rates of CO₂ photoreduction to methane reached the maximum when the exposed face ratio of 58:41 (1.4 μmol h⁻¹ g_{cat}⁻¹; Table 1).

Related to the study, hollow anatase TiO₂ dominating $\{1\ 0\ 1\}$ face was synthesized and the methane formation rate using TiO₂ doped with 1 wt% RuO₂ was by a factor of 1.5 higher than general hollow anatase TiO₂ (Table 2) (14).

1.3. Difference of Reactant Water Phases

The photoreduction CO₂ (200 kPa) with gaseous water (12.3 kPa) and liquid water was compared (Figure 2) (15). Total formation rates of CO and methane using TiO₂ were improved by a factor of 1.7 with gaseous water (1.6 μmol h⁻¹ g_{cat}⁻¹) rather than with liquid water.

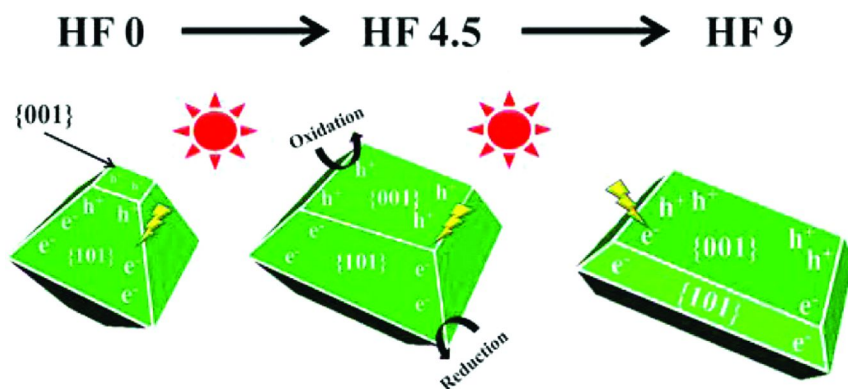


Figure 1. The control of $\{001\}$ and $\{101\}$ exposed face ratio for anatase TiO₂ for photocatalytic CO₂ reduction (13). Reproduced from reference listing (13).

Copyright 2014, ACS.

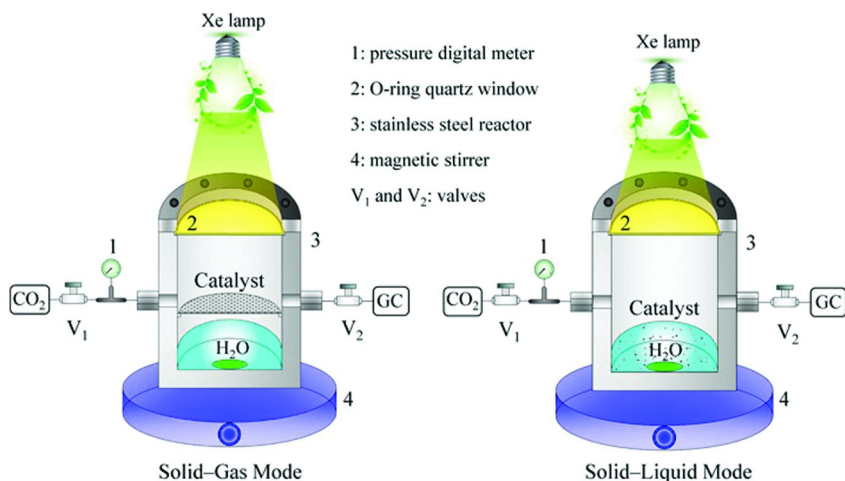


Figure 2. Reactors used for photocatalytic reduction of CO_2 with H_2O . Left: TiO_2 under moisture, right: TiO_2 immersed in liquid water. The distance between the Xe lamp and the catalyst was adjusted to be the same for the two reaction modes (15). Reproduced from reference listing (15). Copyright 2014, ACS.

2. Metal-Loaded TiO_2 Photocatalysts

2.1. Comparisons of Metal

The photoreduction CO_2 (200 kPa) with gaseous water (12.3 kPa) and liquid water was compared (Figure 2) (15). The improvement of total photoreduction rates of CO_2 using Pt- TiO_2 was by a factor of 2.9 ($6.3 \mu\text{mol h}^{-1} \text{g}_{\text{cat}}^{-1}$) (Table 2). This improvement was greater compared to the case for TiO_2 (Table 1). The comparison between solid-gas and solid-liquid interface reactions was also made for CO_2 photoreduction over layered double hydroxide (LDH) photocatalyst (16). The major pathways were CO_2 reduction to methanol and proton reductions to H_2 , respectively.

Total photo-formation rates of methane and CO from CO_2 and gaseous water were in the order:

$$\text{Pt-TiO}_2 (6.3 \mu\text{mol h}^{-1} \text{g}_{\text{cat}}^{-1}) > \text{Pd-TiO}_2 (5.4 \mu\text{mol h}^{-1} \text{g}_{\text{cat}}^{-1}) > \text{Au-TiO}_2 (4.6 \mu\text{mol h}^{-1} \text{g}_{\text{cat}}^{-1}) > \text{Rh-TiO}_2 (4.1 \mu\text{mol h}^{-1} \text{g}_{\text{cat}}^{-1}) > \text{Ag-TiO}_2 (3.8 \mu\text{mol h}^{-1} \text{g}_{\text{cat}}^{-1}) \quad (\text{Table 2})^{15} \quad (8)$$

following the order of work function (WF)

$$\text{Pt} (5.12\text{--}5.93 \text{ eV}) > \text{Pd} (5.22\text{--}5.6 \text{ eV}) > \text{Au} (5.31\text{--}5.47 \text{ eV}) > \text{Rh} (4.98 \text{ eV}) > \text{Ag} (4.52\text{--}4.74 \text{ eV}).^{17} \quad (9)$$

The selectivity for CO₂ photoreduction as compared to H₂O photoreduction to H₂ was 56% using TiO₂, but it decreased to 39–45% by the addition of Pt, Pd, Au, Rh, and Ag because the trapped electrons on these metals thermodynamically preferred to transfer to protons [$E^\circ = 0 - 0.0591 \times \text{pH V}$, versus standard hydrogen electrode (SHE)] rather than both CO₂ and protons ($E^\circ = -0.32 - 0.0591 \times \text{pH V}$, versus SHE) (16).

Solvothermal synthesis of anatase TiO₂ with Ni ions was done and the band gap slightly decreased from 3.16 eV for TiO₂ to 3.00 eV for Ni-TiO₂. Accordingly, photocatalytic production rate of methane from CO₂ increased from 11 (TiO₂) to 14 $\mu\text{mol h}^{-1} \text{g}_{\text{cat}}^{-1}$ (Ni-TiO₂; Table 2) (18). Ni-TiO₂ prepared via sol-gel method, coated on monoliths, and threaded with quartz plate photocatalytically converted CO₂ into methanol at a rate of 20 $\mu\text{mol h}^{-1} \text{g}_{\text{cat}}^{-1}$ (Table 2) (19). The reduction of CO₂ on TiO₂ and oxidation of water on NiO were assumed utilizing the p-n heterojunction.

The effects of Au and Pt loading on TiO₂ were also tested by preparing nanofiber TiO₂ by electrospinning by applying 15 kV between needle for sample precursors and collector (20). Under atmospheric pressure of CO₂ saturated with moisture irradiated by UV-visible light, the TiO₂ nanofiber formed CO and minor methane (Table 1). The selectivity changed to form major methane by the loading of Au (62 $\mu\text{mol h}^{-1} \text{g}_{\text{cat}}^{-1}$) and Pt (84 $\mu\text{mol h}^{-1} \text{g}_{\text{cat}}^{-1}$). The generation rate of methane further improved to 110 $\mu\text{mol h}^{-1} \text{g}_{\text{cat}}^{-1}$ using Au(0.25 atomic%)-Pt(0.75%)-TiO₂ nanofiber (Table 2). Au was metallic state whereas Pt was Pt⁰, Pt²⁺, and Pt⁴⁺ states in these photocatalysts. Electron trap effect due to greater WF for Pt and surface plasmon resonance (SPR) effect at 540–590 nm for Au worked synergetically in the Au(0.25 atomic%)-Pt(0.75%)-TiO₂ nanofiber. The relatively higher formation rates compared to reference (15) would be the difference of amount of photocatalyst used (5 mg (20) versus 20 mg (15)).

Doubly doping of Cu(0.1%) and I(10%) to TiO₂ was effective to photoconvert CO₂ into CO at a rate of 12 $\mu\text{mol h}^{-1} \text{g}_{\text{cat}}^{-1}$ in comparison to that (0.7 $\mu\text{mol h}^{-1} \text{g}_{\text{cat}}^{-1}$) using undoped TiO₂ (Table 2) (21). Double-walled TiO₂ nanotube promoted Cu and Pt with the ratio 1:2 showed good hydrocarbon generation rates of 154–164 $\mu\text{mol h}^{-1} \text{g}_{\text{cat}}^{-1}$ in pressurized CO₂ conditions (Table 2) (22).

The combination of graphene and TiO₂ was reported to effectively form ethane at a formation rate of 17 $\mu\text{mol h}^{-1} \text{g}_{\text{cat}}^{-1}$ (23) and CO at a formation rate of 8.9 $\mu\text{mol h}^{-1} \text{g}_{\text{cat}}^{-1}$ (24) from CO₂ and water (Table 2). Nitrogen-doped TiO₂ was combined with graphitic carbon nitride (g-C₃N₄) (25). The assembly prepared from urea and Ti(OH)₄ with the molar ratio of 7:3 at 853 K was the best to form CO at a rate of 12 $\mu\text{mol h}^{-1} \text{g}_{\text{cat}}^{-1}$ (Table 2). While graphene is regarded as a media to shuttle electrons from TiO₂ (23), g-C₃N₄ (CB minimum: -1.12 V versus SHE) was considered as electron donor to TiO₂ (25).

Table 2. Reported CO₂ Photoreduction Catalysts, Reaction Conditions, and the Formation Rates in Water/with Moisture Using Metal, Metal Oxide, or Other Additive-Loaded TiO₂

<i>Photocatalyst</i>		<i>Reactants</i>		<i>T (K)</i>	<i>Light source</i>	<i>Reactor</i>	<i>Major product {formation rate ($\mu\text{mol h}^{-1} \text{g}_{\text{cat}}^{-1}$)}</i>	<i>Ref</i>
<i>Brand name^a</i>	<i>Amount (mg)</i>	<i>CO₂</i>	<i>H₂O</i>					
RuO ₂ -hollow TiO ₂ {101} major	100	60 kPa		Satur. <i>P</i>	300 W Xe	Teflon lined Stainless	CH ₄ (1.7)	(14)
Pt(0.5%)-P25	20	200 kPa	12.3 kPa	323	100 W Xe	Stainless steel	CH ₄ (5.2), CO (1.1)	(15)
Pd(0.5%)-P25							CH ₄ (4.3), CO (1.1)	(15)
Au(0.5%)-P25							CH ₄ (3.1), CO (1.5)	(15)
Rh(0.5%)-P25							CH ₄ (3.5), CO (0.62)	(15)
Ag(0.5%)-P25							CH ₄ (2.1), CO (1.7)	(15)
MgO(1.0%)- Pt(0.5%)-P25							CH ₄ (11), CO (0.03)	(15)
Pt(0.5%)-P25	20	200 kPa	Liq (4 mL)	323	100 W Xe	Stainless steel	CH ₄ (1.4), CO (0.76)	(15)
Ni-TiO ₂ (anatase)	500	Saturated	Liq (1 L)	303	UV lamp	Pyrex	CH ₄ (14)	(18)
Ni(1.5%)- TiO ₂ monolith	200	Atmosph. <i>P</i>	Satur. <i>P</i>		200 W Hg	Pyrex	CH ₃ OH (20)	(19)
Au(1% ^b)-TiO ₂ nanofiber	5	Atmosph. <i>P</i>	Satur. <i>P</i>		500 W Xe		CH ₄ (62), CO (40)	(20)

<i>Photocatalyst</i>		<i>Reactants</i>		<i>T (K)</i>	<i>Light source</i>	<i>Reactor</i>	<i>Major product {formation rate ($\mu\text{mol h}^{-1} \text{g}_{\text{cat}}^{-1}$)}</i>	<i>Ref</i>
<i>Brand name^a</i>	<i>Amount (mg)</i>	<i>CO₂</i>	<i>H₂O</i>					
Pt(1% ^b)-TiO ₂ nanofiber	5						CH ₄ (84), CO (16)	(20)
Au(0.25% ^b)-Pt(0.75% ^b)- TiO ₂ nanofiber	5						CH ₄ (110), CO (54)	(20)
Cu(0.1%)- I(10%)-TiO ₂	100	Atmosph. <i>P</i>	Satur. <i>P</i>		450 W Xe ($\lambda > 400$ nm)		CO (12)	(21)
Cu-Pt ₂ /TiO ₂ Nanotube	6.7	99.9%	Satur. <i>P</i>	Solar Simulator, AM1.5	High <i>P</i> cell	CH ₄ (120)	CO (12)	(22)
		1.0%	Satur. <i>P</i>				CH ₄ (160)	(22)
graphene(2%)- TiO ₂	100	Atmosph. <i>P</i>	Liq (0.4 mL)		300 W Xe arc	Glass	C ₂ H ₆ (17), CH ₄ (8.0)	(23)
graphene-TiO ₂	10	Atmosph. <i>P</i>	Liq (0.4 mL)		300 W Xe arc		CO (8.9)	(24)
g-C ₃ N ₄ -N- TiO ₂	100	Atmosph. <i>P</i>	Satur. <i>P</i>	303	300 W Xe arc	Teflon	CO (12)	(25)
Pt(0.21% ^b)- TiO ₂	Film	Atmosph. <i>P</i>	Satur. <i>P</i>	Room <i>T</i>	400 W Xe	Stainless steel, Flow	CH ₄ (420)	(26)
Pt(0.94% ^b)- TiO ₂							CH ₄ (1400)	(26)

Continued on next page.

Table 2. (Continued). Reported CO₂ Photoreduction Catalysts, Reaction Conditions, and the Formation Rates in Water/with Moisture Using Metal, Metal Oxide, or Other Additive-Loaded TiO₂

<i>Photocatalyst</i>		<i>Reactants</i>		<i>T (K)</i>	<i>Light source</i>	<i>Reactor</i>	<i>Major product {formation rate ($\mu\text{mol h}^{-1} \text{g}_{\text{cat}}^{-1}$)}</i>	<i>Ref</i>
<i>Brand name^a</i>	<i>Amount (mg)</i>	<i>CO₂</i>	<i>H₂O</i>					
Pt(1.3% ^b)- TiO ₂							CH ₄ (630)	(26)
Pt(2.5% ^b)- TiO ₂							CH ₄ (63)	(26)
Au(1.5%)-P25	50	190 kPa	Satur. <i>P</i>	<333	1000W Xe	Aluminum	CH ₄ (32)	(27)
Au(0.5%)- Cu(1%)-P25	50						CH ₄ (44)	(27)
	25				125 W HP Hg		none	(27)
	25				150 W Xe ($\lambda > 400 \text{ nm}$)		CH ₄ (0.89)	(27)
Cu(1.5%)-P25	50						CH ₄ (40)	(27)
Au(1.5%)-P25	0.6 (1.25 cm ²)						CH ₄ (210)	(27)
Au(0.5%)- Cu(1%)-P25							CH ₄ (2200)	(27)
Cu(1.5%)-P25							CH ₄ (280)	(27)
Cu(bpy) ₂ -P25	100	Gas	Gas		$\lambda > 400 \text{ nm}$		CH ₄ (0.3)	(28)

<i>Photocatalyst</i>		<i>Reactants</i>		<i>T (K)</i>	<i>Light source</i>	<i>Reactor</i>	<i>Major product {formation rate ($\mu\text{mol h}^{-1} \text{g}_{\text{cat}}^{-1}$)}</i>	<i>Ref</i>
<i>Brand name^a</i>	<i>Amount (mg)</i>	<i>CO₂</i>	<i>H₂O</i>					
Cu ₃ (btc) ₂ - core TiO ₂ - shell	300	150 kPa	Liq (5 mL) not immersed	313	300 W Xe arc ($\lambda > 400$ nm)	Stainless steel	CH ₄ (2.6)	(29)
Cu ₃ (btc) ₂	200						none	(29)

^a The loading ratio is weight % except for *b*. ^b Atomic %.

2.2. Effective Thin Layer Photocatalysts

The CO₂ reduction rates using moisture and Pt-supported TiO₂ were improved by the deposition of photocatalyst thin layer (26). Ti(*i*-OC₃H₇)₄ was bubbled by N₂ gas and deposited on indium tin oxide (ITO)-coated glass maintained at 773 K. Then, platinum was sputtered on the TiO₂ film. Based on the images of field-emission scanning electron microscopy (FE-SEM), the TiO₂ film comprised single crystal rods grown on the glass with a typical column diameter of 250 nm and height of 1.5 μm and possessing an orientation of anatase {1 1 2} plane (Figure 3).

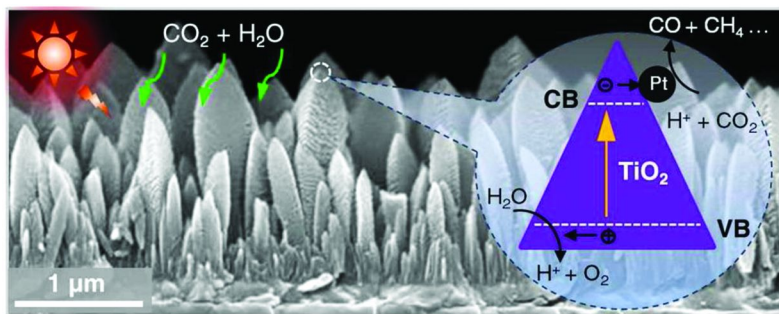


Figure 3. FE-SEM image of thin Pt-TiO₂ film deposited from Ti(*i*-OC₃H₇)₄ and Pt sputtering (26). Reproduced from reference listing (26). Copyright 2012, ACS.

Due to the high dispersion, the TiO₂ film produced CO at higher rate per unit amount of photocatalyst: 240 μmol h⁻¹ g_{cat}⁻¹ from CO₂ and moisture (Table 1). When the Pt atomic % was 0.21, 0.94, 1.3, and 2.5, the average Pt particle size was 0.63, 1.0, 1.3, and 1.9 nm, respectively. By the doping of Pt, the selectivity changed from CO to CH₄. This selectivity change was ascribed that sufficient electrons were accumulated in Pt and thermodynamically stable CH₄ was produced rather than CO. The CH₄ formation rates were maximal at 0.94 atomic % of Pt. By checking the TiO₂ surface coverage of Pt nanoparticles, the increase of methane formation rates until 0.94 atomic % of Pt was ascribed to the increased number of effective Pt sites. The decrease above 0.94 atomic % of Pt was ascribed to particle size effects of Pt. Namely, the reduction potential for Pt nanoparticles is similar to the CB of TiO₂ (≈0 V versus SHE) and electrons excited in CB of TiO₂ would shift to Pt (Figure 4, middle). In contrast, when the Pt nanoparticle size increase at the higher loading, the potential shift to +1.21 V versus SHE as the WF of Pt is 5.65 eV, thereby both electrons and holes tend to shift to Pt and recombine (Figure 4, right) (26).

The CO₂ reduction using moisture and metal-supported TiO₂ was further improved irradiated by 1000 W-Xe lamp, pressurized reactor cell (190 kPa of CO₂), and also the deposition of photocatalyst thin layer (0.6 mg per 1.25 cm²) (27). Using sequentially-deposited and hydrogen-reduced (@673 K) Au(0.5 wt%)-Cu(1.0 wt%)-TiO₂ photocatalyst, methane was formed at a rate of 2200 μmol h⁻¹ g_{cat}⁻¹ (Table 2). In comparison to the performance of Au(1.5 wt%)-TiO₂ and Cu(1.5 wt%)-TiO₂ photocatalysts (210–280 μmol h⁻¹ g_{cat}⁻¹), Au–Cu alloy phase detected in high-resolution transmission electron microscopy (HR-TEM) seemed to be specifically effective. The role of hydrogen-reduced Ti³⁺ sites was also suggested to donate electrons to CO₂.

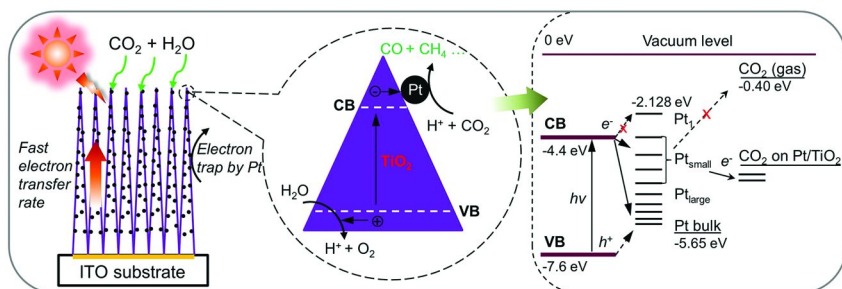


Figure 4. CO₂ photoreduction mechanism using Pt-TiO₂ nanostructured film. The photogenerated electrons move fast inside the highly-oriented TiO₂ single crystals and flow to the Pt nanoparticles, where the reduction reaction occurs to convert CO₂ into CO or CH₄ (middle) (26). Reproduced from reference listing (26). Copyright 2012, ACS.

Using 125-W high-pressure Hg and 150-W Xe lamps (with cutoff filter of $\lambda > 400$ nm) for ultraviolet (UV) and visible irradiations, respectively, for Au-Cu-TiO₂ photocatalyst, no product and methane only were formed, respectively (Table 2) (27). Thus, SPR (the wavelength 570–580 nm) effect of Au in visible light region was suggested to transfer the hot electrons to Cu sites (Figure 5). Carbene pathway was proposed based on Fourier transform infrared (FTIR) rather than formaldehyde pathway (Scheme 1) (5).

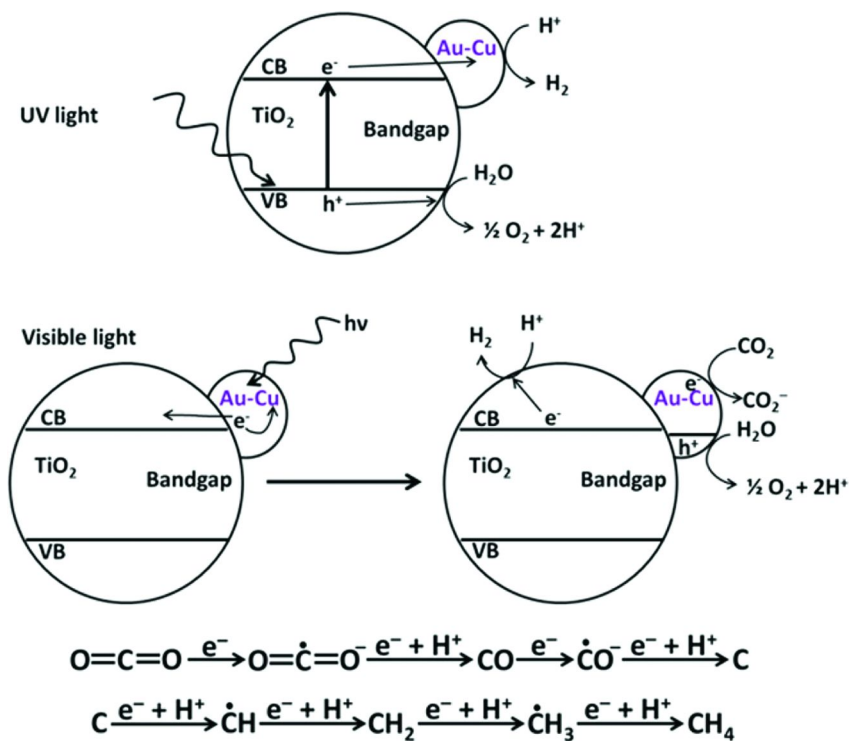
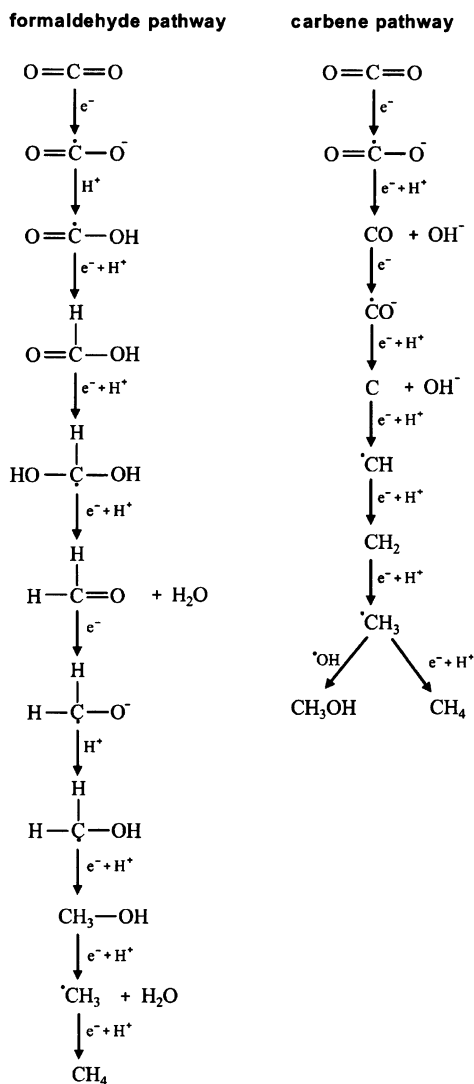


Figure 5. Proposed photocatalytic reaction mechanism of CO₂ reduction with moisture using Au(0.5 wt%)-Cu(1.0 wt%)-TiO₂ photocatalyst (27). Reproduced from reference listing (27). Copyright 2014, ACS.



Scheme 1. Two proposed mechanisms for the photoreduction of CO₂ to methane: formaldehyde (left) and carbene pathways (right) (5). Reproduced from reference listing (15). Copyright 2013, John Wiley and Sons.

3. Metal Oxide or Metal-Organic Framework (MOF)-Loaded TiO₂ Photocatalysts

The Pt-TiO₂ photocatalyst in previous section was further doped with MgO (15). It became methane selective and total formation rate of methane and CO (11 $\mu\text{mol h}^{-1} \text{g}_{\text{cat}}^{-1}$) increased by a factor of 1.8 compared to that using Pt-TiO₂ (Table 2). Doped MgO layer would help CO₂ chemisorption over the catalyst and improve the selectivity for CO₂ reduction versus proton reduction. The Cu bipyridyl (bpy) dye to TiO₂ also promoted the photoreduction of CO₂ to methane at a rate of 0.3 $\mu\text{mol h}^{-1} \text{g}_{\text{cat}}^{-1}$ (Table 2) (28).

The assembly of TiO₂ with MOF was also reported (29). Cu₃(btc)₂ (btc = benzene-1,3,5-tricarboxylate) microcrystals synthesized in the presence of polyvinylpyrrolidone were mixed with tetrabutyl titanate in ethanol and then in HF aqueous solution. By heating at 453 K for 12 h, anatase-phase TiO₂ shells of mean thickness of ~ 200 nm over the Cu₃(btc)₂ cores were formed (Figure 6).

Methane was formed using Cu₃(btc)₂-core|TiO₂-shell from CO₂ and water irradiated by visible light ($\lambda > 400$ nm) at a rate of 2.6 $\mu\text{mol h}^{-1} \text{g}_{\text{cat}}^{-1}$, much higher than than the sum of rates using each component (0.52 and ~ 0 $\mu\text{mol h}^{-1} \text{g}_{\text{cat}}^{-1}$; Tables 1, 2). Exclusive selectivity to methane rather than H₂ was also claimed, probably due to high electron density in the core-shell structure for the eight electron reduction to methane. A 1-ps build-up time in the transient absorption (TA) spectroscopy for the Cu₃(btc)₂-core|TiO₂-shell suggested electron transfer/relaxation from CB of TiO₂ to the interface state with Cu₃(btc)₂ (29).

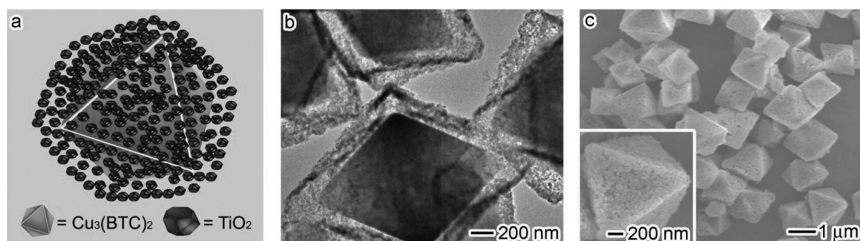


Figure 6. (a) Core-shell structure, (b) TEM, and (c) SEM images of Cu₃(btc)₂@TiO₂ (29). Reproduced from reference listing (29). Copyright 2014, John Wiley and Sons.

4. Semiconductor Photocatalysts Other Than TiO₂

4.1. Photocatalysts Comprising Single Compound

4.1.1. Metal Oxides and Hydroxides

By the irradiation of deep UV light at 185 nm from Hg lamp and using the synthetic quartz windows for the reactor (Figure 7), CO₂ (9.6 kPa) was converted into CH₄ with saturated moisture at a rate of 2.1 $\mu\text{mol h}^{-1}$ for 13.9 h *in the absence of catalyst* (Table 3). It was suggested that water photolysis was the exclusive

hydrogen source for the CO₂ conversion (see *Photon energy conversion of CO₂ to fuels with hydrogen or sacrificial reducing agents, section 1*). The conversion of CO₂ was accelerated (7.7 μmol h⁻¹; Table 3) in the presence of Zn₆Ti LDH (100 mg), but the addition of MgO, TiO₂, CeO₂, or HY-zeolite rather reduced the photocomversion rates of CO₂ (30).

A series of LDHs of [Ni₃M^{III}(OH)₈]₂CO₃·mH₂O, [Mg₃M^{III}(OH)₈]₂CO₃·mH₂O, and [Zn₃M^{III}(OH)₈]₂CO₃·mH₂O (M^{III} = Al, Ga, and In) was tested for CO₂ photoreduction in water (31). [Mg₃M^{III}(OH)₈]₂CO₃·mH₂O was relatively active, e. g. [Mg₃In(OH)₈]₂CO₃·mH₂O produced CO and O₂ at the formation rates of 3.2 and 17 μmol h⁻¹ g_{cat}⁻¹, respectively (Table 3). [Mg₃M^{III}(OH)₈]₂CO₃·mH₂O was selective to form hydrogen whereas [Ni₃M^{III}(OH)₈]₂CO₃·mH₂O was relatively selective to CO formation. The affinity of the surface with CO₂ may be related.

Hexagonal nanoplate-textured micro-octahedron Zn₂SnO₄ as large as a few microns was synthesized and tested for CO₂ photoreduction with 0.4 mL of water (32). Due to its small (quantum) size, the band gap was relative wide (3.87 eV) in which the VB maximum at 2.7 eV and CB minimum at -1.17 eV. The methane formation rate increased from 4.8 to 35 ppm h⁻¹ g_{cat}⁻¹ by loading of 1 wt% of Pt and 1 wt% of RuO₂ to nanoplate-textured micro-octahedron Zn₂SnO₄. KTaO₃ photocatalytically reduced CO₂ with water irradiated by Xe arc lamp to form CO at a rate of 0.34 μmol h⁻¹ g_{cat}⁻¹ (Table 3) (33).

Mesoporous In(OH)₃ photoproducted methane from CO₂ and water at a rate of 0.8 μmol h⁻¹ g_{cat}⁻¹ (Table 3). The rate was by 20 times greater than that using In(OH)₃ without mesoporous structure due to the difference of specific surface area and pore volume (34). Monoclinic Bi₆Mo₂O₁₅ sub-nanowires photocatalyzed CO₂ to methane and the rate was maximal by the preheating at 1073 K. Surface oxygen vacancy created by the heating was considered as an electron trap (35).

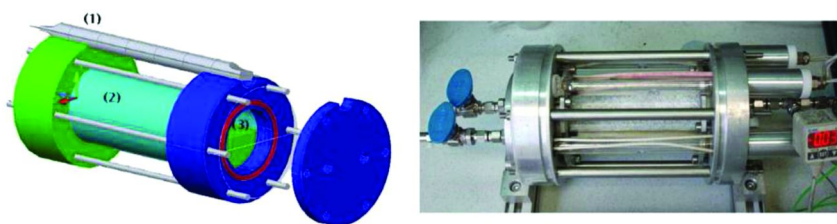


Figure 7. Left: Photoreactor composed by 185 nm-Hg lamp (1), synthetic quartz windows (2), and gas chamber (3). Right: Upper view showing the shallow bed of the photocatalyst placed in the photoreactor (30). Reproduced from reference listing (30). Copyright 2012, ACS.

Table 3. Reported CO₂ Photoreduction Catalysts, Reaction Conditions, and the Formation Rates in Water/with Moisture Using Semiconductor Photocatalysts Other Than TiO₂

<i>Photocatalyst</i>		<i>Reactants</i>		<i>T (K)</i>	<i>Light source</i>	<i>Reactor</i>	<i>Major product {formation rate ($\mu\text{mol h}^{-1} \text{g}_{\text{cat}}^{-1}$)}</i>	<i>Ref</i>
<i>Brand name</i>	<i>Amount (mg)</i>	<i>CO₂</i>	<i>H₂O</i>					
No catalyst	—	9.6 kPa	Satur. <i>P</i>	338	Hg (185, 254 nm)	Quartz	CH ₄ (2.1 ^a)	(30)
KY-zeolite	500						CH ₄ (3.1)	(30)
Zn ₆ Ce LDH	500						CH ₄ (4.3)	(30)
Zn ₆ Ti LDH	500						CH ₄ (3.3)	(30)
Zn ₆ Ti LDH	100						CH ₄ (77)	(30)
Mg ₃ In LDH	100	500 μmol	Liq (4 mL)		200 W Hg-Xe	Quartz	CO (3.2)	(31)
KTaO ₃	100	Atmosph. <i>P</i>	Liq (6 mL)	300 W Xe arc	Borosilicate	CO (0.34)	(33)	
Pt(0.5 %)-In(OH) ₃	200	80 kPa	Liq (2–3 mL)		300 W Xe arc	Circulated	CH ₄ (0.8)	(34)
Graphene Oxide	200	101 kPa	Satur. <i>P</i>	298	300 W halogen	Stainless	CH ₃ OH (0.17)	(36)
g-C ₃ N ₄ (bulk)	20	60 kPa	Liq (0.1 mL)		300 W Xe	Teflon-lined	CH ₃ CHO (3.9)	(37)
g-C ₃ N ₄ (nanosheet)							CH ₄ (4.8)	(37)
CoTe	—	124 kPa	Satur. <i>P</i>	288	300 W Xe ($\lambda > 420 \text{ nm}$)	Quartz	CH ₄ (5.0)	(38)

<i>Photocatalyst</i>		<i>Reactants</i>		<i>T (K)</i>	<i>Light source</i>	<i>Reactor</i>	<i>Major product {formation rate ($\mu\text{mol h}^{-1} \text{g}_{\text{cat}}^{-1}$)}</i>	<i>Ref</i>
<i>Brand name</i>	<i>Amount (mg)</i>	<i>CO₂</i>	<i>H₂O</i>					
ZnTe(3.4%)-ZnO	10	Saturated	Liq (80 mL)	288	300 W Xe arc ($\lambda > 420 \text{ nm}$)	Quartz	CH ₄ (44)	(39)
ZnTe(25%)-SrTiO ₃	20	Atmosph. <i>P</i>	Satur. <i>P</i>		300 W Xe arc ($\lambda > 420 \text{ nm}$)	Quartz	CH ₄ (2.4)	(40)
ZnGa ₂ O ₄	100	Atmosph. <i>P</i>	Liq (0.4 mL)		300 W Xe arc	Glass	CH ₄ (0.26)	(41)
ZnGa ₂ O ₄ :Zn ₂ GeO ₄ (4.5:1)	100						CH ₄ (3.9)	(41)
Zr-Co-Ir-SBA-15	5	101 kPa	13 Pa		355 nm laser		CO (1.7)	(45)
Pt(0.5%)-c-NaNbO ₃	100	80 kPa	Satur. <i>P</i>		300 W Xe arc	Pyrex	CH ₄ (4.9), CO (0.82)	(46)
Pt(0.5%)-o-NaNbO ₃	100						CH ₄ (2.5)	(46)
Pt(0.4%)-Nb ₂ O ₅	100	89 kPa	12 kPa	333	350 W Xe	Quartz	CH ₄ (0.15)	(47)
Pt(0.4%)-HNb ₃ O ₈	100						CH ₄ (0.47)	(47)
Pt(0.4%)-SiO ₂ -HNb ₃ O ₈	100						CH ₄ (2.9)	(47)
Pt(0.4%)-SiO ₂ pillar-HNb ₃ O ₈	100	81 kPa	20 kPa				CH ₄ (3.8)	(47)

Continued on next page.

Table 3. (Continued). Reported CO₂ Photoreduction Catalysts, Reaction Conditions, and the Formation Rates in Water/with Moisture Using Semiconductor Photocatalysts Other Than TiO₂

<i>Photocatalyst</i>		<i>Reactants</i>		<i>T (K)</i>	<i>Light source</i>	<i>Reactor</i>	<i>Major product {formation rate ($\mu\text{mol h}^{-1} \text{g}_{\text{cat}}^{-1}$)}</i>	<i>Ref</i>
<i>Brand name</i>	<i>Amount (mg)</i>	<i>CO₂</i>	<i>H₂O</i>					
InNbO ₄	140	Saturated	0.2M KHCO ₃		500 W halogen	Pyrex	CH ₃ OH (1.4)	(48)
NiO(0.5%)- InNbO ₄	140						CH ₃ OH (1.6)	(48)
Co ₃ O ₄ (1.0%)- InNbO ₄	140						CH ₃ OH (1.5)	(48)
Pt-o-NaNbO ₃	50	Atmosph. <i>P</i>	Liq (4 mL)		300 W Xe arc ($\lambda > 420 \text{ nm}$)	Pyrex vessel	none	(49)
Pt-g-C ₃ N ₄							CH ₄ (0.8)	(49)
Pt-g-C ₃ N ₄ /o- NaNbO ₃							CH ₄ (6.4)	(49)
ZnO-g-C ₃ N ₄	10	400 kPa	Liq (4 mL)	353	500 W Xe ($\lambda >$ 420 nm)	Stainless steel	CO (29)	(50)
Pt(0.5%)-red P-g-C ₃ N ₄	20	Atmosph. <i>P</i>	Liq (0.2 mL)		500 W Xe arc		CH ₄ (300)	(51)
g-C ₃ N ₄							CH ₄ (0.26)	(52)
graphene (15%)-g-C ₃ N ₄							CH ₄ (0.59)	(52)

<i>Photocatalyst</i>		<i>Reactants</i>		<i>T (K)</i>	<i>Light source</i>	<i>Reactor</i>	<i>Major product {formation rate ($\mu\text{mol h}^{-1} \text{g}_{\text{cat}}^{-1}$)}</i>	<i>Ref</i>
<i>Brand name</i>	<i>Amount (mg)</i>	<i>CO₂</i>	<i>H₂O</i>					
RGO(0.5%)- Cu ₂ O	500	Atmosph. <i>P</i>	Liq (3 mL)		150 W Xe	Glass	CO (0.43)	(53)
Ag/AgBr/ CNT	500	7.5 MPa	0.2M KHCO ₃ (100 mL)		150 W Xe ($\lambda >$ 420 nm)	Stainless steel	CH ₄ (30), CH ₃ OH (18), CO (8.0)	(54)

^a μmol of CH₄ h⁻¹.

4.1.2. Carbon-Related Materials

Graphene oxide (GO) with lateral dimension of several micrometers and thickness of 1–3 nm was exfoliated from graphite in acids and tested for CO₂ reduction with moisture irradiated by UV–visible light (36). The methanol formation rate (0.17 μmol h⁻¹ g_{cat}⁻¹) was by a factor of 5.8 higher compared to one using TiO₂ under the reaction conditions (Table 3). The CB minimum estimated for GO (−0.79 V versus SHE) would bend to nearly close to reduction potential from CO₂ to methanol (−0.38 V versus SHE) if the GO with electron-drawing oxygenated functional groups was p-type semiconductor.

Bulk g-C₃N₄ with the Bruanuer–Emmett–Teller surface area (*S*_{BET}) of 50 m² g⁻¹ was compared to g-C₃N₄ nanosheet with *S*_{BET} of 306 m² g⁻¹ (37). Clear difference of selectivity to acetaldehyde and methane (−0.24 V) was observed and one of the major reasons was the difference of band gap (BG), 2.77 and 2.97 eV, respectively. More negative electron potential for the latter sample was considered to effectively reduce CO₂ via glyoxal to acetaldehyde and then to methane (5).

4.1.3. Other Materials

As one of the metal calcogenide compounds, the CB of hydrothermally-synthesized CoTe positioned at relatively negative potential and the BG was 2.05 eV. The methane formation rate using CoTe was 5.0 μmol h⁻¹ g_{cat}⁻¹ (Table 3) (38).

4.2. Assembled Photocatalysts

4.2.1. Zn, Cu-Containing Compounds

The doping of high-potential ZnTe to ZnO was reported (39). The BG of ZnTe was 2.2 eV and the CB minimum was at −1.8 V versus SHE. Due to the excited electrons to CB of ZnO and holes remained at VB of ZnTe, methane was formed irradiated by visible light ($\lambda > 420$ nm). ZnTe was a sensitizer for visible light, but the reason of quite high formation rate (44 μmol h⁻¹ g_{cat}⁻¹; Table 3) from CO₂ to methane via electron transfer from CB of ZnO is not known and control reaction tests are needed. High-potential ZnTe was also combined with SrTiO₃ and formed methane from CO₂ and moisture (Table 3) (40).

The performance of CO₂ photoreduction to methane using cubic spinel ZnGa₂O₄ was improved by mixing pseudo cubic inverse spinel Zn₂GeO₄ from 0.26 to 3.9 μmol h⁻¹ g_{cat}⁻¹ (Table 3) (41). One of the reasons was suggested to be the reduction of band gap from 4.45 to 4.18 eV to utilize wider spectrum of light (42).

Zn-doped (100)-oriented p-GaP was utilized for CO₂ photoreduction with water irradiated by a laser light at 532 nm. To prevent the photocorrosion of GaP, atomic layer deposition of Ti chloride and water vapor was performed to

create 1–10 nm-thick TiO₂ layers over GaP (43). Methanol was formed on the GaP photoelectrode covered with 5 nm-thick TiO₂ at a rate of 1.2 μmol h⁻¹ cm_{cat}⁻² at the applied voltage of -0.5 V (versus SHE) in 0.5 M NaCl and 10 mM pyridine solution. Thin TiO₂ layer seemed not just the passivation layer to transmit the light at 532 nm, but also to serve to form p–n junction for charge separation (43).

Cu₂O electrodeposited on CuO nanorods perpendicularly grown on Cu foil photoreduced CO₂ in CO₂-saturated 0.1 M Na₂SO₄ aqueous solution at the electric potential smaller than 0.37 V (versus SHE) irradiated by simulated AM 1.5 light. The geometry of CuO nanorod and Cu₂O shell should facilitate charge separation irradiated by light and CO₂ reduction on CuO (44).

4.2.2. Zr, Co, Ir-Containing Compounds

Stepwise synthesis of photoreduction sites of CO₂ and photooxidation sites of water in single sample was reported. Zirconocene dichloride was reacted with an ordered mesoporous SiO₂, SBA-15, to form Zr-SBA-15 (45). The Co precursor preferably reacted with Zr–OH group to form links of Zr^{IV}–O–Co^{II} in Zr(1.1 mol%)-Co(0.7 mol%)-SBA-15. Ir^{III} acetylacetonate was photodeposited on Zr-Co-SBA-15, but not on Zr-SBA-15 and Co-SBA-15, suggesting electron transfer by the irradiation of 355 nm laser light from Co to Zr (Zr^{III}–O–Co^{III}) coupled with the electron transfer from Ir to Co (Ir^{III}···O–Co^{II} → Ir^{IV}–O–Co^{II}). Though the Ir^{IV}–O–Co^{II} link may be lost upon calcination later than the electrodeposition, Zr^{IV}–O–Co^{II} and IrO_x nanocluster were formed in the vicinity over SBA-15.

The CO formation at a rate of 1.7 μmol h⁻¹ g_{cat}⁻¹ under 101 kPa of CO₂ and 13 Pa of water irradiated by laser at 355 nm (127 mW cm⁻²; Table 3) was ascribed to water oxidation on IrO_x nanocluster and the resultant electron transfer to neighboring Co^{II} and then to Zr^{IV} (45). Spectroscopic insight for the interaction of Zr^{III} and CO₂ would be expected.

4.2.3 Nb-Containing Compounds

Two phases of perovskite-type NaNbO₃ doped with 0.5 wt% of Pt were tested (Table 3) (46). One is cubic NaNbO₃ (c-NaNbO₃) and the other is more common orthorhombic NaNbO₃ (o-NaNbO₃). The Pt-c-NaNbO₃ photocatalyst produced major methane (4.9 μmol h⁻¹ g_{cat}⁻¹) and minor CO (0.82 μmol h⁻¹ g_{cat}⁻¹) from gaseous CO₂ and moisture, and the methane formation rate was by a factor 2.0 greater compared to that using Pt-o-NaNbO₃. Two reasons of the difference was suggested to be (1) minor difference of band gap value and (2) homogeneous frontier orbital [highest occupied molecular orbital (MO), lowest unoccupied MO] distribution in *x*, *y*, *z*-direction for c-NaNbO₃ versus the distorted distribution in *z*-direction for o-NaNbO₃.

Pt-photodeposited layered HNb₃O₈ was superior to Pt-photodeposited layered KNb₃O₈ for CO₂ photoreduction at 333 K (47). The methane formation rates were improved to 3.8 μmol h⁻¹ g_{cat}⁻¹ when the moisture pressure increased from 12 to

20 kPa and also SiO₂ pillared between the layers of HNb₃O₈ (Table 3). However, not O₂ or H₂ was detected in the study, suggesting incomplete photocatalytic cycle.

For InNbO₄, the doping of NiO (0.5%) or Co₃O₄ (1.0%) slightly promoted the methanol photoformation (1.6–1.5 μmol h⁻¹ g_{cat}⁻¹) from CO₂ compared to unpromoted one (1.4 μmol h⁻¹ g_{cat}⁻¹; Table 3) (48).

4.2.4 C-Containing Compounds

o-NaNbO₃ nanowire was combined with polymeric g-C₃N₄ (49). Methane was photogenerated using Pt-g-C₃N₄/NaNbO₃ at a rate of 6.4 μmol h⁻¹ g_{cat}⁻¹ higher by a factor of 8 compared to that using Pt-g-C₃N₄ (Table 3). Pt-o-NaNbO₃ was inert in the conditions. The advantage of Pt-g-C₃N₄/NaNbO₃ was ascribed to the charge separation at the heterojunction of p-type g-C₃N₄ to attract holes and n-type NaNbO₃ to attract excited electrons.

g-C₃N₄ was also combined with ZnO (50) and red-P (51) to form heterojunction and converted CO₂ into major CO and major methane at rates of 29 and 300 μmol h⁻¹ g_{cat}⁻¹, respectively. The reason of quite high methane formation rate using red-P-g-C₃N₄ is unclear and control reaction tests are needed.

The disadvantages, low electric conductivity and rapid recombination of photogenerated electrons and holes, of 2-dimensional(D) g-C₃N₄ for photocatalysis were solved by assembling graphene with g-C₃N₄ (52). The electrons at N 2p was photoexcited to C 2p (CB: -1.42 V versus SHE) in g-C₃N₄ and could move to conducting network graphene (Fermi level: -0.08 V versus SHE). Thus, CO₂ photoreduction rate into methane was boosted from 0.26 μmol h⁻¹ g_{cat}⁻¹ (g-C₃N₄) to 0.59 μmol h⁻¹ g_{cat}⁻¹ for graphene (15 wt%)-g-C₃N₄ assembly (Table 3).

Cu₂O assembled with 0.5 wt% of reduced graphene oxide (RGO) was also reported. CO was produced from CO₂ and water at a rate of 0.43 μmol h⁻¹ g_{cat}⁻¹ (Table 3) (53). Similar to reference 44, negative potential of CB for Cu₂O (-1.44 V versus SHE, pH 0) should be advantageous for electron donation toward CO₂-derived species.

A part of Ag⁺ of AgBr/carbon nanotube (CNT) was photoreduced to form Ag/AgBr/CNT (54). The photocatalyst was immersed in weak alkaline solution pressurized with 7.5 MPa of CO₂. Methane, methanol, and CO were formed at a total formation rate of 56 μmol h⁻¹ g_{cat}⁻¹ (Table 3). Longer CNT was preferable than shorter one probably due to better charge separation efficiency.

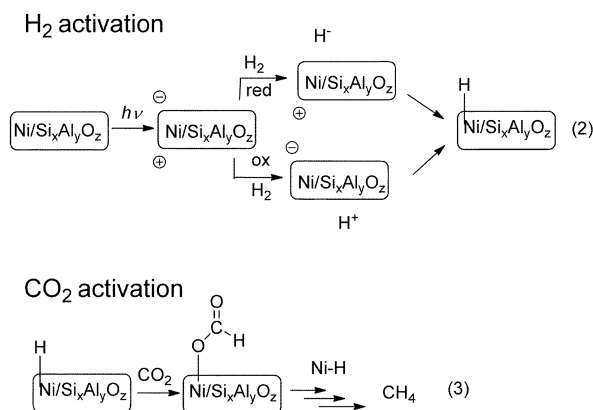
Photon Energy Conversion of CO₂ to Fuels with Hydrogen or Sacrificial Reducing Agents

1. Photon Energy Conversion of CO₂ to Fuels with Hydrogen

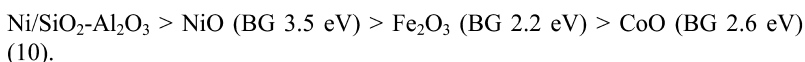
If oxidation of water produces O₂, protons, and electrons, utilizing natural light, photon energy conversion of CO₂ to fuels with hydrogen (H atom equivalent to a proton and an electron) is also important as a latter half cycle of artificial photosynthesis (4).

By the irradiation of deep UV light at 185 nm from Hg lamp and using synthetic quartz windows for the reactor, CO₂ (9.6 kPa) was converted into major CH₄ and minor CO with H₂ (45 kPa) at a rate of 4.5 μmol h⁻¹ for 82 h *in the absence of catalyst* (Table 4) (30). This rate was faster than the photolysis of CO₂ with water (*see Photon energy conversion of CO₂ to fuels with water, section 4.1.1*; Table 3). Light of 185 nm was confirmed to be responsible for the photolysis of CO₂ rather than light of 254 nm from the Hg lamp.

High conversion of CO₂ with H₂ was reported using Ni/SiO₂-Al₂O₃ in similar reactor to Figure 7 at a methane formation rate of 55 mmol h⁻¹ g_{cat}⁻¹ (Table 4) (55). By the effects of high-power solar simulator and heat of reaction for CO₂ hydrogenation to methane (165 kJ mol⁻¹), the temperature reached 423 K and gas pressure would be some hundreds kPa. Control experiment at 453 K in dark formed methane at significantly lower rate of 8.9 μmol h⁻¹ g_{cat}⁻¹. Thus, the photocatalytic reduction was photoactivated and accompanied by thermal catalytic step(s). Ni/SiO₂-Al₂O₃ when UV light was filtered showed similar activity to NiO irradiated by UV-visible light (13 mmol h⁻¹ g_{cat}⁻¹; Table 4). The performance irradiated under UV-visible light was in the order



Scheme 2. Proposed reaction mechanism of photocatalytic CO₂ reduction with H₂ presumably assisted by later thermal catalytic step(s) using Ni/SiO₂-Al₂O₃ (55). Reproduced from reference listing (55). Copyright 2014, ACS.



It was difficult to find the direct relationship between the reactivity and BG values or the conduction band level. Instead, formation of active Ni-H species was proposed by reducing/oxidizing H₂ to H⁻/H⁺ and reacting with Ni⁺/Ni⁻, respectively (Scheme 2) (55).

Table 4. Reported CO₂ Photoreduction Catalysts, Reaction Conditions, and the Formation Rates Using Various Semiconductors with Hydrogen

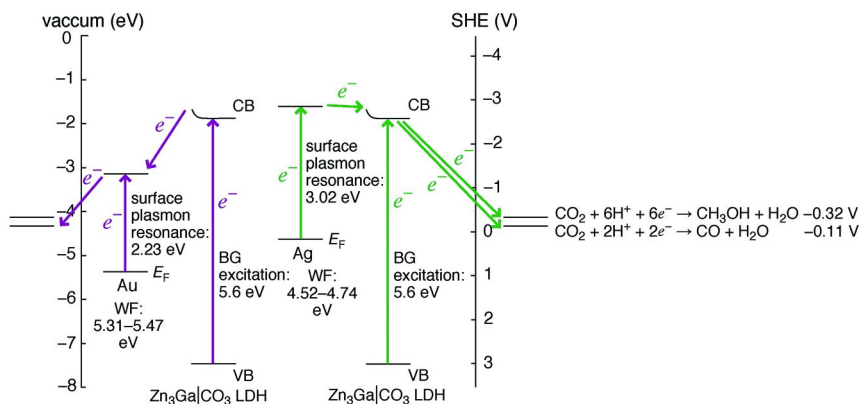
<i>Photocatalyst</i>		<i>Reactants</i>		<i>T (K)</i>	<i>Light source</i>	<i>Reactor</i>	<i>Major product {formation rate ($\mu\text{mol h}^{-1} \text{g}_{\text{cat}}^{-1}$)}</i>	<i>Ref</i>
<i>Brand name</i>	<i>Amount (mg)</i>	<i>CO₂</i>	<i>H₂</i>					
No catalyst	—	9.6 kPa	45 kPa	338 K	Hg (185, 254 nm)	Quartz	CH ₄ (4.5 ^a)	(30)
Ni/SiO ₂ -Al ₂ O ₃	250	3.7 mmol	17 mmol	<423	Solar simulator (AM1.5 filter)	Aluminum	CH ₄ (55 000)	(55)
NiO							CH ₄ (13 000)	(55)
Fe ₂ O ₃							CO (7 200)	(55)
CoO							CO (2 500), CH ₄ (1 600)	(55)
Ni/SiO ₂ -Al ₂ O ₃	250	3.7 mmol	17 mmol		Solar simulator (λ > 420 nm)	Aluminum	CH ₄ (13 000)	(55)
NiO							CH ₄ (210), CO (170)	(55)
Zn ₃ Ga CO ₃ LDH	100	2.3 kPa	21.7 kPa	<313	500 W Xe arc	Pyrex	CO (0.08), CH ₃ OH (0.05)	(56)
Ag(0.36%)- Zn ₃ Ga CO ₃ LDH	100	2.3 kPa	21.7 kPa	<313	500 W Xe arc	Pyrex	CH ₃ OH (0.12), CO (0.10)	(57)
Au(4.1%)- Zn ₃ Ga CO ₃ LDH	100	2.3 kPa	21.7 kPa	<313	500 W Xe arc	Pyrex	CO (0.20), CH ₃ OH (0.03)	(57)

<i>Photocatalyst</i>		<i>Reactants</i>		<i>T (K)</i>	<i>Light source</i>	<i>Reactor</i>	<i>Major product {formation rate ($\mu\text{mol h}^{-1} \text{g}_{\text{cat}}^{-1}$)}</i>	<i>Ref</i>
<i>Brand name</i>	<i>Amount (mg)</i>	<i>CO₂</i>	<i>H₂</i>					
CuPcTs- Zn ₃ Ga CO ₃ LDH	100	2.3 kPa	21.7 kPa	<313	500 W Xe arc	Pyrex	CO (0.11), CH ₃ OH (0.096)	(58)
Zn ₃ Ga Cu(OH) ₄ LDH	100	2.3 kPa	21.7 kPa	<313	500 W Xe arc	Pyrex	CH ₃ OH (0.30), CO (0.13)	(60)

^a $\mu\text{mol of CH}_4 \text{ h}^{-1}$.

A LDH $[\text{Zn}_3\text{Ga}(\text{OH})_8]_2\text{CO}_3 \cdot m\text{H}_2\text{O}$ ($m \sim 4$; Zn_3Ga) exhibited direct electronic transition and the BG value was 5.6 eV (56). This wide-BG LDH was combined with SPR of Ag and Au nanoparticles (Scheme 3) (57). The SPR peaks appeared in visible light region centered at 411 and 555 nm, respectively. By the irradiation of UV-visible light, the total formation rates of CO and methanol using Zn_3Ga LDH ($0.13 \mu\text{mol h}^{-1} \text{g}_{\text{cat}}^{-1}$) increased to $0.22 \mu\text{mol h}^{-1} \text{g}_{\text{cat}}^{-1}$ using Ag/ Zn_3Ga LDH and to $0.23 \mu\text{mol h}^{-1} \text{g}_{\text{cat}}^{-1}$ using Au/ Zn_3Ga LDH. The selectivity to methanol was also improved from 39 to 54 mol% (Table 4) by the doping of Ag, whereas the Au doped led to selective CO formation (13 mol%).

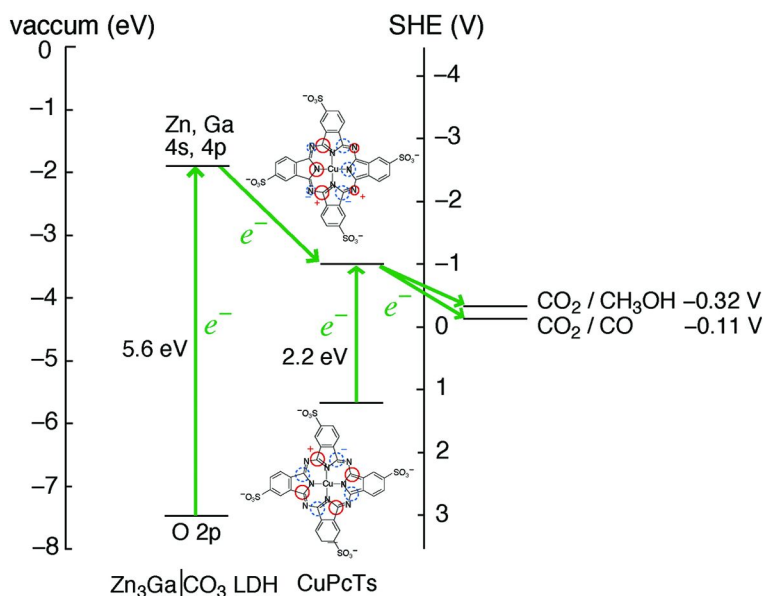
Ag/ Zn_3Ga LDH and Cu phthalocyanine tetrasulfonate (PcTs)-doped Zn_3Ga LDH were active irradiated by visible light ($\lambda > 420 \text{ nm}$; total formation rate 0.12 and $0.15 \mu\text{mol h}^{-1} \text{g}_{\text{cat}}^{-1}$, respectively) (57, 58). The mechanism could be explained by the electron shift due to SPR in Ag to wide-BG Zn_3Ga LDH then to CO_2 -derived species (Scheme 3, right) and electron shift from wide-band gap Zn_3Ga LDH to LUMO of CuPcTs then to CO_2 -derived species (Scheme 4). Conversely, as the WF of Au was larger than that for Ag (17), the electrons could not be supplied to the CB of LDH (Scheme 3, left). Thus, Au worked as electron trap from LDH irradiated by UV light and SPR in Au was ineffective for CO_2 photoreduction (57). The electron flows originating from SPR were in consistent with charge transfer mechanism reviewed previously (59).



Scheme 3. The energy diagram and proposed electron flows in Ag/ Zn_3Ga LDH (right) and Au/ Zn_3Ga LDH (left) (57). Reproduced from reference listing (57).

Copyright 2015, Elsevier.

The CO₂ photoreduction ability of [Zn_{1.5}Cu_{1.5}Ga(OH)₈]₂CO₃·mH₂O (Figure 8A) was also improved by the interlayer anion substitution by [Cu(OH)₄]²⁻ for CO₃²⁻ (Figure 8B) (60). Especially, methanol formation rates increased from 0.05 to 0.30 μmol h⁻¹ g_{cat}⁻¹ by the anion substitution (Table 4). X-ray absorption near-edge structure (XANES) was applied to monitor the diffusion of photogenerated electrons to active Cu^{II} sites as the 1s-3d pre-edge peak intensity (61). Electron diffusion to Cu sites was an order of magnitude faster in the direction of the cationic layers of [Zn_{1.5}Cu_{1.5}Ga(OH)₈]₂CO₃·mH₂O (580 μmol h⁻¹ g_{cat}⁻¹; Figure 8A) than in the perpendicular direction to interlayer [Cu(OH)₄]²⁻ in [Zn₃Ga(OH)₈]₂[Cu(OH)₄]·mH₂O (36 μmol h⁻¹ g_{cat}⁻¹; Figure 8B) (61, 62). With the information of FTIR, selective methanol formation mechanism via hydrogen carbonate (bicarbonate) and step-by-step reduction with proton and electron was proposed using [Zn₃Ga(OH)₈]₂[Cu(OH)₄]·mH₂O LDH (Scheme 5).



Scheme 4. The energy diagram and proposed electron flows in CuPcTs/Zn₃Ga LDH.

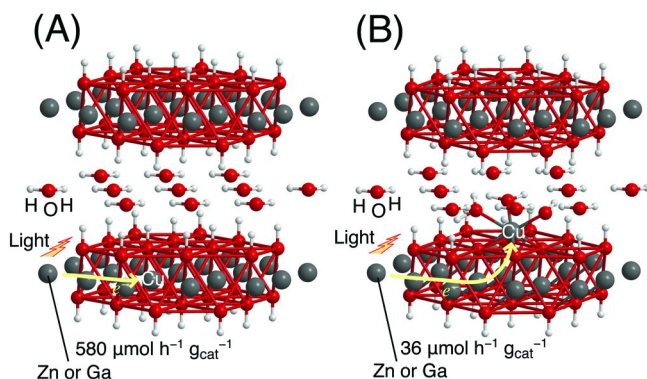
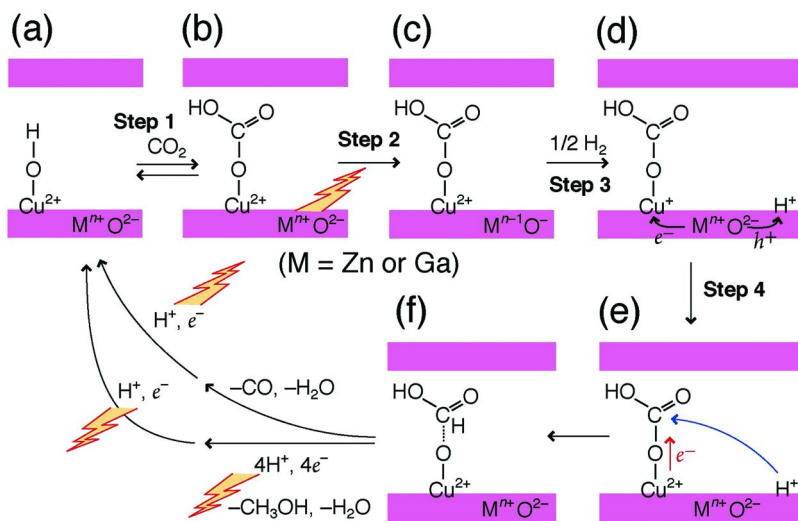


Figure 8. Structure of $[Zn_{1.5}Cu_{1.5}Ga(OH)_8]_2CO_3 \cdot mH_2O$ (A) and structure of $[Zn_3Ga(OH)_8]_2[Cu(OH)_4] \cdot mH_2O$ (B). Interlayer carbonates are not drawn in (A) for clarity (62). Reproduced from reference listing (62). Copyright 2014, High-Energy Accelerator Research Organization.



Scheme 5. Proposed photocatalytic cycle of CO_2 reduction to methanol or CO using LDH catalysts comprising Zn, Ga, and interlayer Cu sites (61). Reproduced from reference listing (61). Copyright 2014, Elsevier.

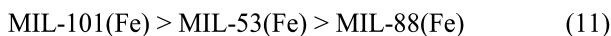
2. Photon Energy Conversion of CO_2 to Fuels with Other Sacrificial Reducing Agents than H_2

CO_2 photoreduction into major CO using Au_3Cu alloy on $SrTiO_3/TiO_2$ nanotubes and hydrous hydrazine was reported at a formation rate of $730 \mu mol h^{-1} g_{cat}^{-1}$ (Table 5) (63). Cuboid Cu_2O powder was superior ($20 ppm h^{-1} g_{cat}^{-1}$) to octahedral Cu_2O for CO_2 photoreduction to CO in water and the rate was by several times enhanced by the addition of 0.25 wt% of RuO_x using Na_2SO_3 as sacrificial reducing agent (64).

Na₂SO₃ was also used as sacrificial reducing agent, and the CO₂ pressure to water suspension of Au-TiO₂ was raised to 1.0 MPa at 298 K. The methane generation rate increased to 20 μmol h⁻¹ g_{cat}⁻¹ (Table 5) (65). Methanol was used as sacrificial reducing agent, and the generation rates of methyl formate from CO₂ was in the order using hexagonal ZnIn₂S₄ > cubic ZnIn₂S₄ > microspheric ZnIn₂S₄ (Table 5) (66).

The progress of MOF as photocatalysts for CO₂ reduction was fast in these three years. MIL-101(Fe) comprising Fe₃O clusters linked by terephthalates to form quasi-spherical cages produced formate at a rate of 150 μmol h⁻¹ g_{cat}⁻¹ in the presence of triethanol amine (TEOA) as reducing agent from dissolved CO₂ in acetonitrile irradiated by visible light (420 < λ < 800 nm; Table 5) (67). MIL-53(Fe) comprising chains of hydroxy corner-sharing FeO₆ octahedra linked by terephthalates to form 1D pores and MIL-88(Fe) comprising oxo-centered Fe₃O clusters linked by terephthalates to form 3D porous network were less active (74–23 μmol h⁻¹ g_{cat}⁻¹) compared to MIL-101(Fe) (Table 5). The electron transfer from O²⁻ to Fe³⁺ irradiated by visible light was proposed as the first step for the CO₂ reduction.

When 2-aminoterephthalic acid was used for the syntheses of MOF's above, the generation rates of formate were improved to 450–75 μmol h⁻¹ g_{cat}⁻¹ compared to MIL's unfunctionalized by the amine group (150–23 μmol h⁻¹ g_{cat}⁻¹; Table 5). Amine group significantly extended the UV absorption edge toward visible region, and proposed to create second electron transfer pass from NH₂ to Fe-O center. The flat band position for MIL-101(Fe), MIL-53(Fe), and MIL-88(Fe) were -0.52, -0.70, and -0.48 V, respectively, versus SHE. The values were clearly more negative than the reduction potential of CO₂ to formate (-0.28 V), however, the order of photocatalysis



was not correlated to the flat band potential (67).

A combination of Zn-containing MOF (called ZIF-8) and Zn₂GeO₄ was reported (68). In aqueous solution with 0.1 M Na₂SO₃ aqueous solution saturated with CO₂, methanol was photogenerated at a rate of 0.22 μmol h⁻¹ g_{cat}⁻¹ (Table 5). A Co-containing MOF, Co-ZIF-9, was tested with the aid of CdS photocatalyst and sacrificial reductant, TEOA irradiated by visible light (69). CO was formed at a rate of 2400 μmol h⁻¹ g_{cat}⁻¹ (Table 5). Co ions in ZIF-9 was suggested to received excited electrons in CdS.

5,10,15,20-Tetrakis(4-carboxyphenyl)porphyrin coordinated to Al³⁺ to form MOF. The methanol formation rate from CO₂ utilizing triethylamine (TEA; 38 ppm h⁻¹ g_{cat}⁻¹) was improved by introducing Cu²⁺ to the porphyrin in the MOF (260 ppm h⁻¹ g_{cat}⁻¹; Table 5) (70). The surface of GO was carboxylated and was functionalized with -CH₂-COCl and then reacted with Co phthalocyanine tetrasulfonamide (71). Sensitization by CoPc and transferred electrons to GO were suggested to reduce CO₂ into methanol at a rate of 79 μmol h⁻¹ g_{cat}⁻¹ compared to 39 μmol h⁻¹ g_{cat}⁻¹ using unsensitized GO by using TEA as sacrificial reductant (Table 5).

Table 5. Reported CO₂ Photoreduction Catalysts, Reaction Conditions, and the Formation Rates with Sacrificial Reducing Agents

<i>Photocatalyst</i>		<i>Reactants</i>		<i>T (K)</i>	<i>Light source</i>	<i>Reactor</i>	<i>Major product {formation rate ($\mu\text{mol h}^{-1} \text{g}_{\text{cat}}^{-1}$)}</i>	<i>Ref</i>
<i>Brand name</i>	<i>Amount (mg)</i>	<i>CO₂</i>	<i>Reducing agent</i>					
Au ₃ Cu/ SrTiO ₃ /TiO ₂	5	33.7 kPa	N ₂ H ₄ ·H ₂ O		300 W Xe		CO (730)	(63)
Cu ₂ O	500	Saturated	0.7 M Na ₂ SO ₃		300 W Xe ($\lambda > 350 \text{ nm}$)	Glass	CO	(64)
Au(0.1%)- TiO ₂	500	1.0 MPa	Na ₂ SO ₃	298	125 W Hg	High <i>P</i> cell	CH ₄ (20)	(65)
hex-ZnIn ₂ S ₄	10	Saturated	CH ₃ OH	298	250 W Hg		MF (190)	(66)
cub-ZnIn ₂ S ₄							MF (160)	
sph-ZnIn ₂ S ₄							MF (50)	
MIL-101(Fe)	50	Saturated in CH ₃ CN	TEOA		300 W Xe (420 < λ < 800 nm)	Flask	HCO ₂ ⁻ (150)	(67)
MIL-53(Fe)							HCO ₂ ⁻ (74)	(67)
MIL-88(Fe)							HCO ₂ ⁻ (23)	(67)
NH ₂ -MIL- 101(Fe)							HCO ₂ ⁻ (450)	(67)
NH ₂ -MIL- 53(Fe)							HCO ₂ ⁻ (120)	(67)
NH ₂ -MIL- 88(Fe)							HCO ₂ ⁻ (75)	(67)

<i>Photocatalyst</i>		<i>Reactants</i>		<i>T (K)</i>	<i>Light source</i>	<i>Reactor</i>	<i>Major product {formation rate ($\mu\text{mol h}^{-1} \text{g}_{\text{cat}}^{-1}$)}</i>	<i>Ref</i>
<i>Brand name</i>	<i>Amount (mg)</i>	<i>CO₂</i>	<i>Reducing agent</i>					
Zn ₂ GeO ₄ -ZIF-8	200	Saturated	Liq (100 mL), 0.1 M Na ₂ SO ₃		500 W Xe arc		CH ₃ OH (0.22)	(68)
CdS-Co-ZIF-9 20, 1		101 kPa	TEOA (1 mL)	303	300 W Xe ($\lambda > 420$ nm)		CO (2400)	(69)
Al-porphyrin MOF	30	Atmosph. P	TEA (1 mL)	278	300 W Xe ($\lambda > 420$ nm)		CH ₃ OH	(70)
Al-Cu-porphyrin MOF							CH ₃ OH	(70)
GO	100		TEA (10 mL)		20 W white cold LED	Borosil	CH ₃ OH (39)	(71)
CoPc-GO							CH ₃ OH (79)	(71)

Photon Energy Conversion of CO₂ to Fuels Using Combination System with Photooxidation Catalysts

Although the homogeneous photocatalysts and enzymes for CO₂ reduction are out of scope of this chapter that is limiting to semiconductor photocatalysts, several studies were reported/reviewed to combine homogeneous complex or enzyme for CO₂ photoreduction with semiconductor photocatalyst, e.g. Ru bpy-like complex with Ag/TaON (72, 73).

The phenomena of photocatalytic oxidation of water and photocatalytic reduction of CO₂ were combined using a cell (Figure 9A), in which the two photocatalysts, WO₃ and [Zn_{1.5}Cu_{1.5}Ga(OH)₈]₂[Cu(OH)₄]_mH₂O LDH, were separated by a polymer electrolyte (PE) film (Figure 9B) (16). WO₃ was used for the photooxidation of water, whereas Zn–Cu–Ga LDH was used for the photoreduction of CO₂. Protons and electrons, which were formed on WO₃ under the flow of moisture (solid–gas interface mode; Figure 9B), were used on Zn–Cu–Ga LDH instead of reactant H₂ in *Photon energy conversion of CO₂ to fuels with hydrogen or sacrificial reducing agent, section 1* (56–58, 60). For this process, photocatalysts pressed on both sides of the PE film were irradiated by UV–visible light through quartz windows and through the space in carbon electrode plates set for both gas flow and light transmission. Methanol was the major product on LDH at a formation rate of 0.045 μmol h⁻¹ g_{cat}⁻¹ under the flow of CO₂ (Table 6). This rate accounted for 68–100% of photocurrents between the two redox photoelectrodes.

In comparison, liquid-type another cell, which consisted of WO₃ and LDH immersed in acidic solutions, with the PE film distinguishing the two compartments was reported (Figure 9C). The photocurrent from LDH to WO₃ was increased by 2.4–3.4 times in comparison to gas–solid mode cell (Figure 9B) tested under similar conditions. However, major product from LDH was H₂ at a formation rate of 0.67 μmol h⁻¹ g_{cat}⁻¹. The difference of phase of water (moisture in panel B, liquid in panel C; Figure 9) directed the selectivity to methanol (equation 12) versus H₂ (equation 13) (16). This trend of phase difference was in consistent with that found for metal-loaded TiO₂ (*Photon energy conversion of CO₂ to fuels with water, section 2.1*) (15).



Using a similar tandem twin reactor separated by PE film, CO₂ conversion to methanol was also reported at rates of 1.6–1.8 μmol h⁻¹ g_{cat}⁻¹ using WO₃ on photoanode and Pt(1 wt%)-CuAlGaO₄ and/or Pt(0.8 %)-SrTiO₃:Rh on photocathode (74). A clear difference to reference 16 was the photocatalysts were not mounted on electrode and redox mediator (Fe³⁺ in anode and Fe²⁺ in cathode) was used. However, it is not certain whether electrons or Fe²⁺ would transfer through the PE film.

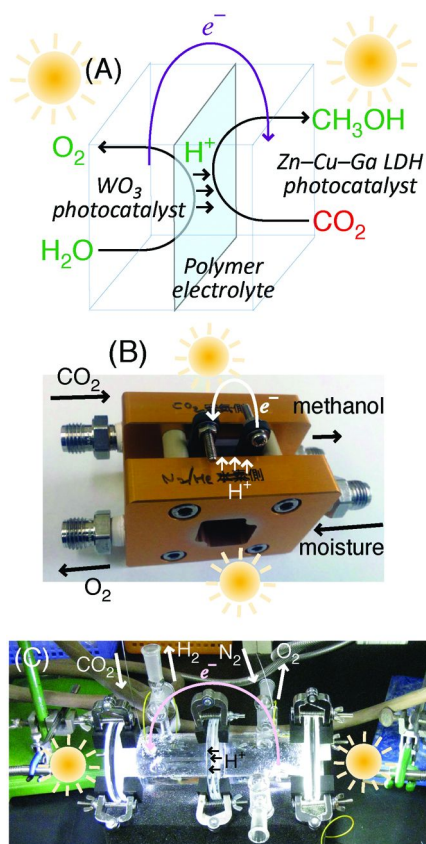


Figure 9. The reaction path in photofuel cell (A), cell-1 to flow moisture to WO_3 (B, front) and to circulate CO_2 to LDH (B, back), and cell-2 to flow N_2 to WO_3 (C, right) and CO_2 to LDH (C, left) immersed in HCl solutions (16). Reproduced from reference listing (16). Copyright, 2014, The Royal Society of Chemistry.

Table 6. Reported CO₂ Photoreduction Catalysts, Reaction Conditions, and the Formation Rates Combined with Photooxidation Catalysts

<i>Photocatalyst</i>		<i>Reactants</i>		<i>T (K)</i>	<i>Light source</i>	<i>Reactor</i>	<i>Major product {formation rate ($\mu\text{mol h}^{-1} \text{g}_{\text{cat}}^{-1}$)}</i>	<i>Ref</i>
<i>Brand name</i>	<i>Amount (mg)</i>	<i>CO₂</i>	<i>H₂O</i>					
anode:								
WO ₃	95	(Ne/N ₂)	Satur. P	< 315	500 W Xe arc	PEFC		(16)
cathode:								
Zn _{1.5} Cu _{1.5} Ga Cu(OH) ₄	45	3.5 kPa					CH ₃ OH (0.045)	
anode:								
WO ₃	300	(Ar)	225 mL (Fe ³⁺ : 2mM)		300 W Xe	Twin R separated by PE		(74)
cathode:								
Pt(1 %)-CuAlGaO ₄	300	Saturated	(Fe ²⁺ : 2mM)				CH ₃ OH (1.8)	
anode:								
WO ₃	300							(74)
cathode:								
Pt(1 %)-CuAl- GaO ₄ ,	150						CH ₃ OH (1.6)	
Pt(0.8 %)-SrTiO ₃ :Rh	150							

Concluding Remarks

Recent advances in photocatalytic CO₂ conversion with water and/or other reductants in these three years were reviewed in comparison to classic studied prior to 2012 (4) using TiO₂ (75–81), ZnO (81), CdS (81), GaP (81), SiC (81), WO₃ (81), Zn₂GeO₄ (82), Bi₂WO₆ (83), HNb₃O₈ (84), CuGa_{1-x}Fe_xO₂ (85), A^{II}La₄Ti₄O₁₅ (86), [Zn_{1.5}Cu_{1.5}Ga(OH)₈]₂CO₃·*m*H₂O (56, 60), ZrO₂ (87), GaP (81, 88), GaAs (88, 89), and InP (89). Starting from CO₂ and water, methane or CO formation using TiO₂ was improved to 0.1–17 μmol h⁻¹ g_{cat}⁻¹ by choosing appropriate crystalline phase (brookite or anatase), crystalline face, and the defects. Metals, e.g. Pt, Pd, Au, Rh, Ag, Ni, Cu, Au₃Cu alloy, I, MgO, RuO₂, graphene, g-C₃N₄, Cu-containing dyes, and Cu-containing MOFs were effective to assist TiO₂ to form methane, CO, methanol, or ethane at rates of 1.4–160 μmol h⁻¹ g_{cat}⁻¹ and further to 32–2200 μmol h⁻¹ g_{cat}⁻¹ if minimal thin photocatalyst film was well deposited.

Semiconductors, e.g. ZnO, Zn₆Ti LDH, Mg₃In LDH, KTaO₃, graphene, GO, g-C₃N₄, CoTe, TiO₂-coated p-GaP, Zn₂SnO₄, ZnO, ZnTe, SrTiO₃, ZnGa₂O₄, Zn₂GeO₄, Zr–Co–Ir oxides, Nb₂O₅, HNbO₃, NaNbO₃, KNb₃O₈, InNbO₄, NiO, Co₃O₄, Cu₂O, and their assemblies were effective to photogenerate methane, CO, methanol, acetaldehyde at rates of 0.15–300 μmol h⁻¹ g_{cat}⁻¹ in good competition with promoted TiO₂.

If H₂ was used, new photoactivation of CO₂ followed by thermal assisted reaction(s) was reported using Ni/SiO₂-Al₂O₃ to produce methane at 423 K under pressurized CO₂ + H₂ at a rate of 55 mmol h⁻¹ g_{cat}⁻¹ presumably via Ni–H species. As pure photocatalytic reaction, methanol formation rates were improved up to 0.30 μmol h⁻¹ g_{cat}⁻¹ by the doping of Ag/Au nanoparticles, [Cu(OH)₄]²⁻ anions, and Cu-containing dyes to Zn–Ga LDH. The combination of two semiconductors (WO₃, Zn–Cu–Ga LDH) were reported to form methanol at a rate of 0.05 μmol h⁻¹ g_{cat}⁻¹ from CO₂ and gaseous water.

In this chapter, the improvement of CO₂ conversion and new materials for the photoreduction were focused, and the importance of wavelength (deep UV, UV, and visible light) and flux of incident light, temperature, and form (powder, nanofiber, and/or film) of photocatalysts, pressure of reactants, were critical to determine the photoconversion of CO₂ for the stage of new energy application levels. To enable the optimum reaction and photocatalyst conditions, the importance of reactor cell (30, 55) was also suggested.

However, reaction mechanisms of CO₂ activation, e.g. via glyoxal (9), via O-defect to form CO (equations 3–5) (10), multiple-step formaldehyde pathway (5), multiple-step carbene pathway (5, 27), via metal–H active species (55), and via hydrogen carbonate (bicarbonate) (56, 61), are still in debate. To clarify the mechanism and responsible sites, spectroscopic studies, e.g. FTIR (27, 45, 61, 67, 70), diffuse reflectance infrared Fourier transform (10), electron paramagnetic resonance (9, 67), FE-SEM (22, 26, 49, 57), HR-TEM (20, 26, 27, 46, 47, 49, 54), photoluminescence (15), action (in-profile) spectrum (55, 57, 58), time-resolved TA (26, 29, 55), valence X-ray photoelectron (35, 39, 49), XANES (57, 61), EXAFS (90), and density functional theory calculations (9, 13, 29, 34, 46) are inevitable.

Acknowledgments

The authors are grateful for the financial supports from the Grant-in-Aid for Scientific Research C (26410204, 22550117) from Japan Science Promotion Agency, the Feasibility Study Stage of A-STEP (Proposal Nos. AS262Z00159L, AS251Z00906L, AS231Z01459C) from the Japan Science and Technology Agency, the Iwatani Naoji Foundation, Asahi Glass Foundation, the Promotion Section of Technology Innovation, Daikin Industries, and approval of the Photon Factory Proposal Review Committee for X-ray measurements (2014G631, 2011G033, 2009G552) for research related to this chapter.

References

1. Lewis, N.; Nocera, D. G. Powering the Planet: Chemical Challenges in Solar Energy Utilization. *Proc. Nat. Acad. Sci.* **2006**, *103*, 15729–15735.
2. Bolton, J. R. Solar Photoproduction of Hydrogen: A Review. *Solar Ener.* **1996**, *57*, 37–50.
3. Aresta, M.; Dibenedetto, A.; Angelini, A. Catalysis for the Valorization of Exhaust Carbon: from CO₂ to Chemicals, Materials, and Fuels. Technological Use of CO₂. *Chem. Rev.* **2014**, *114*, 1709–1742.
4. Izumi, Y. Recent Advances in the Photocatalytic Conversion of Carbon Dioxide to Fuels with Water and/or Hydrogen Using Solar Energy and Beyond. *Coord. Chem. Rev.* **2013**, *257*, 171–186.
5. Habisreutinger, S. N.; Schmidt-Mende, L.; Stolarczyk, J. K. Photocatalytic Reduction of CO₂ on TiO₂ and Other Semiconductors. *Angew. Chem., Int. Ed.* **2013**, *52*, 7372–7408.
6. Smestad, G. P.; Steinfeld, A. Review: Photochemical and Thermochemical Production of Solar Fuels from H₂O and CO₂ Using Metal Oxide Catalysts. *Ind. Eng. Chem. Res.* **2012**, *51*, 11828–11840.
7. Roy, S. C.; Varghese, O. K.; Paulose, M.; Grimes, C. A. Toward Solar Fuels: Photocatalytic Conversion of Carbon Dioxide to Hydrocarbons. *ACS Nano* **2010**, *4*, 1259–1278.
8. Indrakanti, V. P.; Kubicki, J. D.; Schobert, H. H. Photoinduced Activation of CO₂ on Ti-based Heterogeneous Catalysts: Current State, Chemical Physics-based Insights and Outlook. *Ener. Environ. Sci.* **2009**, *2*, 745–758.
9. Dimitrijevic, N. M.; Vijayan, B. K.; Poluektov, O. G.; Rajh, T.; Gray, K. A.; He, H.; Zapol, P. Role of Water and Carbonates in Photocatalytic Transformation of CO₂ to CH₄ on Titania. *J. Am. Chem. Soc.* **2011**, *133*, 3964–3971.
10. Liu, L.; Zhao, H.; Andino, J. M.; Li, Y. Photocatalytic CO₂ Reduction with H₂O on TiO₂ Nanocrystals: Comparison of Anatase, Rutile, and Brookite Polymorphs and Exploration of Surface Chemistry. *ACS Catal.* **2012**, *2*, 1817–1828.
11. Zhao, H.; Liu, L.; Andino, J. M.; Li, Y. Bicrystalline TiO₂ with Controllable anatase–Brookite Phase Content for Enhanced CO₂ Photoreduction to Fuels. *J. Mater. Chem. A* **2013**, *1*, 8209–8216.

12. Ye, L.; Mao, J.; Peng, T.; Zan, L.; Zhang, Y. Opposite Photocatalytic Activity Orders of Low-Index Facets of Anatase TiO₂ for Liquid Phase Dye Degradation and Gaseous Phase CO₂ Photoreduction. *Phys. Chem. Chem. Phys.* **2014**, *16*, 15675–15680.
13. Yu, J.; Low, J.; Xiao, W.; Zhou, P.; Jaroniec, M. Enhanced Photocatalytic CO₂-Reduction Activity of Anatase TiO₂ by Coexposed {001} and {101} Facets. *J. Am. Chem. Soc.* **2014**, *136*, 8839–8842.
14. Jiao, W.; Wang, L.; Liu, G.; Lu, G. Q.; Cheng, H. M. Hollow Anatase TiO₂ Single Crystals and Mesocrystals with Dominant {101} Facets for Improved Photocatalysis Activity and Tuned Reaction Preference. *ACS Catal.* **2012**, *2*, 1854–1859.
15. Xie, S.; Wang, Y.; Zhang, Q.; Deng, W.; Wang, Y. MgO- and Pt-Promoted TiO₂ as an Efficient Photocatalyst for the Preferential Reduction of Carbon Dioxide in the Presence of Water. *ACS Catal.* **2014**, *4*, 3644–3653.
16. Morikawa, M.; Ogura, Y.; Ahmed, N.; Kawamura, S.; Mikami, G.; Okamoto, S.; Izumi, Y. Photocatalytic Conversion of Carbon Dioxide into Methanol in Reverse Fuel Cells with Tungsten Oxide and Layered Double Hydroxide Photocatalysts for Solar Fuel Generation. *Catal. Sci. Technol.* **2014**, *4*, 1644–1651.
17. Weast, R. C. *CRC Handbook of Chemistry and Physics*; CRC Press: Boca Raton, FL, 2001; vol. 82; pp 12–130.
18. Kwak, B. S.; Vignesh, K.; Park, N. K.; Ryu, H. J.; Baek, J. I.; Kang, M. Methane Formation from Photoreduction of CO₂ with Water Using TiO₂ Including Ni Ingredient. *Fuel* **2015**, *143*, 570–576.
19. Ola, O.; Maroto-Valer, M. M. Role of Catalyst Carriers in CO₂ Photoreduction over Nanocrystalline Nickel Loaded TiO₂-based Photocatalysts. *J. Catal.* **2014**, *309*, 300–308.
20. Zhang, Z.; Wang, Z.; Cao, S. W.; Xue, C. Au/Pt Nanoparticle-Decorated TiO₂ Nanofibers with Plasmon-Enhanced Photocatalytic Activities for Solar-to-Fuel Conversion. *J. Phys. Chem. C* **2013**, *117*, 25939–25947.
21. Zhang, Q.; Gao, T.; Andino, J. M.; Lio, Y. Copper and Iodine Co-modified TiO₂ nanoparticles for Improved Activity of CO₂ Photoreduction with Water Vapor. *Appl. Catal. B* **2012**, *123/124*, 257–264.
22. Zhang, X.; Han, F.; Shi, B.; Farsinezhad, S.; Dechaine, G. P.; Shankar, K. Photocatalytic Conversion of Diluted CO₂ into Light Hydrocarbons Using Periodically Modulated Multiwalled Nanotube Arrays. *Angew. Chem., Int. Ed.* **2012**, *51*, 12732–12735.
23. Tu, W.; Zhou, Y.; Liu, Q.; Yan, S.; Bao, S.; Wang, X.; Xiao, M.; Zou, Z. An In Situ Simultaneous Reduction-Hydrolysis Technique for Fabrication of TiO₂-Graphene 2D Sandwich-Like Hybrid Nanosheet: Graphene-Promoted Selectivity of Photocatalytic-Driven Hydrogenation and Coupling of CO₂ into Methane and Ethane. *Adv. Funct. Mater.* **2013**, *23*, 1743–1749.
24. Tu, W.; Zhou, Y.; Liu, Q.; Tian, Z.; Gao, J.; Chen, X.; Zhang, H.; Liu, J.; Zou, Z. Robust Hollow Spheres Consisting of Alternating Titania Nanosheets and Graphene Nanosheets with High Photocatalytic Activity for CO₂ Conversion into Renewable Fuels. *Adv. Funct. Mater.* **2012**, *22*, 1215–1221.

25. Zhou, S.; Liu, Y.; Li, J.; Wang, Y.; Jiang, G.; Zhao, Z.; Wang, D.; Duan, A.; Liu, J.; Wei, Y. Facile In Situ Synthesis of Graphitic Carbon Nitride (g-C₃N₄)-N-TiO₂ Heterojunction as an Efficient Photocatalyst for the Selective Photoreduction of CO₂ to CO. *Appl. Catal., B* **2014**, *158/159*, 20–29.
26. Wang, W. N.; An, W. J.; Ramalingam, B.; Mukherjee, S.; Niedzwiedzki, D. M.; Gangopadhyay, S.; Biswas, P. Size and Structure Matter: Enhanced CO₂ Photoreduction Efficiency by Size-Resolved Ultrafine Pt Nanoparticles on TiO₂ Single Crystals. *J. Am. Chem. Soc.* **2012**, *134*, 11276–11281.
27. Neațu, Ș.; Maciá-Agulló, J. A.; Concepción, P.; Garcia, H. Gold–Copper Nanoalloys Supported on TiO₂ as Photocatalysts for CO₂ Reduction by Water. *J. Am. Chem. Soc.* **2014**, *136*, 15969–15976.
28. Yuan, Y. J.; Yu, Z. T.; Zhang, J. Y.; Zou, Z. G. A Copper(I) Dye-Sensitized TiO₂-Based System for Efficient Light Harvesting and Photoconversion of CO₂ into Hydrocarbon Fuel. *Dalton Trans.* **2012**, *41*, 9594–9597.
29. Li, R.; Hu, J.; Deng, M.; Wang, H.; Wang, X.; Hu, Y.; Jiang, H. L.; Jiang, J.; Zhang, Q.; Xie, Y.; Xiong, Y. Integration of an Inorganic Semiconductor with a Metal–Organic Framework: A Platform for Enhanced Gaseous Photocatalytic Reactions. *Adv. Mater.* **2014**, *26*, 4783–4788.
30. Sastre, F.; Corma, A.; Garcia, H. 185 nm Photoreduction of CO₂ to Methane by Water. Influence of the Presence of a Basic Catalyst. *J. Am. Chem. Soc.* **2012**, *134*, 14137–14141.
31. Teramura, K.; Iguchi, S.; Mizuno, Y.; Shishido, T.; Tanaka, T. Photocatalytic Conversion of CO₂ in Water over Layered Double Hydroxides. *Angew. Chem. Int. Ed.* **2012**, *51*, 8008–8011.
32. Li, Z.; Zhou, Y.; Zhang, J.; Tu, W.; Liu, Q.; Yu, T.; Zou, Z. Hexagonal Nanoplate-Textured Micro-Octahedron Zn₂SnO₄: Combined Effects toward Enhanced Efficiencies of Dye-Sensitized Solar Cell and Photoreduction of CO₂ into Hydrocarbon Fuels. *Crys. Growth Des.* **2012**, *12*, 1476–1481.
33. Li, K.; Handoko, A. D.; Khraisheh, M.; Tang, J. Photocatalytic Reduction of CO₂ and Protons Using Water as an Electron Donor over Potassium Tantalate Nanoflakes. *Nanoscale* **2014**, *6*, 9767–9773.
34. Guo, J.; Ouyang, S.; Kako, T.; Ye, J. Mesoporous In(OH)₃ for Photoreduction of CO₂ into Renewable Hydrocarbon Fuels. *Appl. Surf. Sci.* **2013**, *280*, 418–423.
35. Li, P.; Zhou, Y.; Tu, W.; Wang, R.; Zhang, C.; Liu, Q.; Li, H.; Li, Z.; Dai, H.; Wang, J.; Yan, S.; Zou, Z. Synthesis of Bi₆Mo₂O₁₅ Sub-Microwires via a Molten Salt Method and Enhancing the Photocatalytic Reduction of CO₂ into Solar Fuel through Tuning the Surface Oxide Vacancies by Simple Post-Heating Treatment. *Crys. Eng. Commun.* **2013**, *15*, 9855–9858.
36. Hsu, H. C.; Shown, I.; Wei, H. Y.; Chang, Y. C.; Du, H. Y.; Lin, Y. G.; Tseng, C. A.; Wang, C. H.; Chen, L. C.; Lin, Y. C. Graphene Oxide as a Promising Photocatalyst for CO₂ to Methanol Conversion. *Nanoscale* **2013**, *5*, 262–268.
37. Niu, P.; Yang, Y.; Yu, J. C.; Liu, G.; Cheng, H. M. Switching the Selectivity of the Photoreduction Reaction of Carbon Dioxide by Controlling the Band Structure of a g-C₃N₄ Photocatalyst. *Chem. Commun.* **2014**, *50*, 10837–10840.

38. Khan, M. S.; Ashiq, M. N.; Ehsan, M. F.; He, T.; Ijaz, S. Controlled Synthesis of Cobalt Telluride Superstructures for the Visible Light Photo-conversion of Carbon Dioxide into Methane. *Appl. Catal., A* **2014**, *487*, 202–209.
39. Ehsan, M. F.; He, T. In Situ Synthesis of ZnO/ZnTe Common Cation Heterostructure and Its Visible-Light Photocatalytic Reduction of CO₂ into CH₄. *Appl. Catal., B* **2015**, *166/167*, 345–352.
40. Ehsan, M. F.; Ashiq, M. N.; Bi, F.; Palanisamy, S.; He, T. Preparation and Characterization of SrTiO₃-ZnTe Nanocomposites for the Visible-Light Photoconversion of Carbon Dioxide to Methane. *RSC Adv.* **2014**, *4*, 48411–48418.
41. Yan, S.; Wang, J.; Gao, H.; Wang, N.; Yu, H.; Li, Z.; Zhou, Y.; Zou, Z. Zinc Gallogermanate Solid Solution: A Novel Photocatalyst for Efficiently Converting CO₂ into Solar Fuels. *Adv. Funct. Mater.* **2013**, *23*, 1839–1845.
42. Blankenship, R. E.; Tiede, D. M.; Barber, J.; Brudvig, G. W.; Fleming, G.; Ghirardi, M.; Gunner, M. R.; Junge, W.; Kramer, D. M.; Melis, A.; Moore, T. A.; Moser, C. C.; Nocera, D. G.; Nozik, A. J.; Ort, D. R.; Parson, W. W.; Prince, R. C.; Sayre, R. T. Comparing Photosynthetic and Photovoltaic Efficiencies and Recognizing the Potential for Improvement. *Science* **2011**, *332*, 805–809.
43. Zeng, G.; Qiu, J.; Li, Z.; Pavaskar, P.; Cronin, S. B. CO₂ Reduction to Methanol on TiO₂-Passivated GaP Photocatalysts. *ACS Catal.* **2014**, *4*, 3512–3516.
44. Ghadimkhani, G.; de Tacconi, N. R.; Chanmanee, W.; Janaky, C.; Rajeshwar, K. Efficient Solar Photoelectrosynthesis of Methanol from Carbon Dioxide Using Hybrid CuO–Cu₂O Semiconductor Nanorod Arrays. *Chem. Commun.* **2013**, *49*, 1297–1299.
45. Kim, W.; Yuan, G.; McClure, B. A.; Frei, H. Light Induced Carbon Dioxide Reduction by Water at Binuclear ZrOCo^{II} Unit Coupled to Ir Oxide Nanocluster Catalyst. *J. Am. Chem. Soc.* **2014**, *136*, 11034–11042.
46. Li, P.; Ouyang, S.; Xi, G.; Kako, T.; Ye, J. The Effects of Crystal Structure and Electronic Structure on Photocatalytic H₂ Evolution and CO₂ Reduction over Two Phases of Perovskite-Structured NaNbO₃. *J. Phys. Chem. C* **2012**, *116*, 7621–7628.
47. Li, X.; Li, W.; Zhuang, Z.; Zhong, Y.; Li, Q.; Wang, L. Photocatalytic Reduction of Carbon Dioxide to Methane over SiO₂-Pillared HNb₃O₈. *J. Phys. Chem. C* **2012**, *116*, 16047–16053.
48. Lee, D. S.; Chen, H. J.; Chen, Y. W. Photocatalytic Reduction of Carbon Dioxide with Water Using InNbO₄ Catalyst with NiO and Co₃O₄ Cocatalysts. *J. Phys. Chem. Solid* **2012**, *73*, 661–669.
49. Shi, H.; Chen, G.; Zhang, C.; Zou, Z. Polymeric g-C₃N₄ Coupled with NaNbO₃ Nanowires toward Enhanced Photocatalytic Reduction of CO₂ into Renewable Fuel. *ACS Catal.* **2014**, *4*, 3637–3643.
50. He, Y.; Wang, Y.; Zhang, L.; Teng, B.; Fan, M. High-Efficiency Conversion of CO₂ to Fuel over ZnO/g-C₃N₄ Photocatalyst. *Appl. Catal., B* **2015**, *168/169*, 1–8.

51. Yuan, Y. P.; Cao, S. W.; Liao, Y. S.; Yin, L. S.; Xue, C. Red Phosphor/g-C₃N₄ Heterojunction with Enhanced Photocatalytic Activities for Solar Fuel Production. *Appl. Catal., B* **2013**, *140/141*, 164–168.
52. Ong, W. J.; Tan, L. L.; Chai, S. P.; Yong, S. T. Graphene Oxide as a Structure-Directing Agent for the Two-Dimensional Interface Engineering of Sandwich-Like Graphene–g-C₃N₄ Hybrid Nanostructures with Enhanced Visible-Light Photoreduction of CO₂ to Methane. *Chem. Commun.* **2015**, *51*, 858–861.
53. An, X.; Li, K.; Tang, J. Cu₂O/Reduced Graphene Oxide Composites for the Photocatalytic Conversion of CO₂. *ChemSusChem* **2014**, *7*, 1086–1093.
54. Asi, M. A.; Zhu, L.; He, C.; Sharma, V. K.; Shu, D.; Li, S.; Yang, J.; Xiong, Y. Visible-Light-Harvesting Reduction of CO₂ to Chemical Fuels with Plasmonic Ag@AgBr/CNT Nanocomposites. *Catal. Today* **2013**, *216*, 268–275.
55. Sastre, F.; Puga, A. V.; Liu, L.; Corma, A.; García, H. Complete Photocatalytic Reduction of CO₂ to Methane by H₂ under Solar Light Irradiation. *J. Am. Chem. Soc.* **2014**, *136*, 6798–6801.
56. Ahmed, N.; Shibata, Y.; Taniguchi, T.; Izumi, Y. Photocatalytic Conversion of Carbon Dioxide into Methanol Using Zinc–Copper–M(III) (M = Aluminum, Gallium) Layered Double Hydroxides. *J. Catal.* **2011**, *279*, 123–135.
57. Kawamura, S.; Puscasu, M. C.; Yoshida, Y.; Izumi, Y.; Carja, G. Tailoring Assemblies of Plasmonic Silver/Gold and Zinc–Gallium Layered Double Hydroxides for Photocatalytic Conversion of Carbon Dioxide Using UV–Visible Light. *Appl. Catal. A* **2015** DOI:10.1016/apcata.2014.12.042.
58. Kawamura, S.; Ahmed, N.; Morikawa, M.; Mikami, G.; Carja, G.; Izumi, Y. Photocatalytic Conversion of Carbon Dioxide Using Zn–Cu–Al or Ga Layered Double Hydroxides: Cu in Contact with Gaseous Reactant is Needed for Methanol Generation. *Oil Gas Sci. Technol.* **2015** May 5 in press.
59. Hou, W.; Cronin, S. B. A Review of Surface Plasmon Resonance-Enhanced Photocatalysis. *Adv. Funct. Mater.* **2013**, *23*, 1612–1619.
60. Ahmed, N.; Morikawa, M.; Izumi, Y. Photocatalytic Conversion of Carbon Dioxide into Methanol Using Optimized Layered Double Hydroxide Catalysts. *Catal. Today* **2012**, *185*, 263–269.
61. Morikawa, M.; Ahmed, N.; Yoshida, Y.; Izumi, Y. Photoconversion of Carbon Dioxide in Zinc–Copper–Gallium Layered Double Hydroxides: The Kinetics to Hydrogen Carbonate and Further to CO/Methanol. *Appl. Catal., B* **2014**, *144*, 561–569.
62. Izumi, Y.; Kawamura, S.; Morikawa, M.; Naveed, A. Monitoring of Electron Flow in Layered Double Hydroxides to Photoreduce Carbon Dioxide into Fuels; Photon Factory Activity Report 2013 (Highlights); 2014; Vol. 31A, pp 36–37. , *31A*, 36–37.
63. Kang, Q.; Wang, T.; Li, P.; Liu, L.; Chang, K.; Li, M.; Ye, J. Photocatalytic Reduction of Carbon Dioxide by Hydrous Hydrazine over Au–Cu Alloy Nanoparticles Supported on SrTiO₃/TiO₂ Coaxial Nanotube Arrays. *Angew. Chem. Int. Ed.* **2015**, *54*, 841–845.

64. Handoko, A. D.; Tang, J. Controllable Proton and CO₂ Photoreduction over Cu₂O with Various Morphologies. *Int. J. Hydrogen Energy* **2013**, *38*, 13017–13022.
65. Rossetti, I.; Villa, A.; Pirola, C.; Prati, L.; Ramis, G. A Novel High-Pressure Photoreactor for CO₂ Photoconversion to Fuels. *RSC Adv.* **2014**, *4*, 28883–28885.
66. Chen, J.; Xin, F.; Yin, X.; Xiang, T.; Wang, Y. *RSC Adv.* **2015**, *5*, 3833–3839.
67. Wang, D.; Huang, R.; Liu, W.; Sun, D.; Li, Z. Fe-Based MOFs for Photocatalytic CO₂ Reduction: Role of Coordination Unsaturated Sites and Dual Excitation Pathways. *ACS Catal.* **2014**, *4*, 4254–4260.
68. Liu, Q.; Low, Z. X.; Li, L.; Razmjou, A.; Wang, K.; Yao, J.; Wang, H. ZIF-8/Zn₂GeO₄ Nanorods with an Enhanced CO₂ Adsorption Property in an Aqueous Medium for Photocatalytic Synthesis of Liquid Fuel. *J. Mater. Chem. A* **2013**, *1*, 11563–11569.
69. Wang, S.; Wang, X. Photocatalytic CO₂ Reduction by CdS Promoted with a Zeolitic Imidazolate Framework. *Appl. Catal., B* **2015**, *162*, 494–500.
70. Liu, Y.; Yang, Y.; Sun, Q.; Wang, Z.; Huang, B.; Dai, Y.; Qin, X.; Zhang, X. Chemical Adsorption Enhanced CO₂ Capture and Photoreduction over a Copper Porphyrin Based Metal Organic Framework. *ACS Appl. Mater. Interfaces* **2013**, *5*, 7654–7658.
71. Kumar, P.; Kumar, A.; Sreedhar, B.; Sain, B.; Ray, S. S.; Jain, S. L. Cobalt Phthalocyanine Immobilized on Graphene Oxide: An Efficient Visible-Active Catalyst for the Photoreduction of Carbon Dioxide. *Chem. Eur. J.* **2014**, *20*, 6154–6161.
72. Sekizawa, K.; Maeda, K.; Domen, K.; Koide, K.; Ishitani, O. Artificial Z-Scheme Constructed with a Supramolecular Metal Complex and Semiconductor for the Photocatalytic Reduction of CO₂. *J. Am. Chem. Soc.* **2013**, *135*, 4596–4599.
73. Windle, C. D.; Perutz, R. N. Advances in Molecular Photocatalytic and Electrocatalytic CO₂ Reduction. *Coord. Chem. Rev.* **2012**, *256*, 2562–2570.
74. Lee, W. H.; Liao, C. H.; Tsai, M. F.; Huang, C. W.; Wu, J. C. S. A Novel Twin Reactor for CO₂ Photoreduction to Mimic Artificial Photosynthesis. *Appl. Catal., B* **2013**, *132/133*, 445–451.
75. Yui, T.; Kan, A.; Saitoh, C.; Koide, K.; Ibusuki, T.; Ishitani, O. Photochemical Reduction of CO₂ Using TiO₂: Effects of Organic Adsorbates on TiO₂ and Deposition of Pd onto TiO₂. *ACS Appl. Mater. Interfaces* **2011**, *3*, 2594–2600.
76. Yang, C. C.; Yu, Y. H.; van der Linden, B.; Wu, J. C. S.; Mul, G. Artificial Photosynthesis over Crystalline TiO₂-Based Catalysts: Fact or Fiction? *J. Am. Chem. Soc.* **2010**, *132*, 8398–8406.
77. Varghese, O. K.; Paulose, M.; LaTempa, T. J.; Grimes, C. A. High-Rate Solar Photocatalytic Conversion of CO₂ and Water Vapor to Hydrocarbon Fuels. *Nano Lett.* **2009**, *9*, 731–737.
78. Tseng, I. H.; Chang, W. C.; Wu, J. C. S. Photoreduction of CO₂ Using Sol-Gel Derived Titania and Titania-Supported Catalysts. *Appl. Catal., B* **2002**, *37*, 37–48.

79. Kaneco, S.; Kurimoto, H.; Shimizu, Y.; Ohta, K.; Mizuno, T. Photocatalytic Reduction of CO₂ Using TiO₂ Powders in Supercritical Fluid CO₂. *Energy* **1999**, *24*, 21–30.
80. Anpo, M.; Yamashita, H.; Ichihashi, Y.; Fujii, Y.; Honda, M. Photocatalytic Reduction of CO₂ with H₂O on Titanium Oxides Anchored within Micropores of Zeolites: Effects of the Structure of the Active Sites and the Addition of Pt. *J. Phys. Chem. B* **1997**, *101*, 2632–2636.
81. Inoue, T.; Fujishima, A.; Konishi, S.; Honda, K. Photoelectrocatalytic Reduction of Carbon Dioxide in Aqueous Suspensions of Semiconductor Powders. *Nature* **1979**, *277*, 637–638.
82. Liu, Q.; Zhou, Y.; Kou, J.; Chen, X.; Tian, Z.; Gao, J.; Yan, S.; Zou, Z. High-Yield Synthesis of Ultralong and Ultrathin Zn₂GeO₄ Nanoribbons toward Improved Photocatalytic Reduction of CO₂ into Renewable Hydrocarbon Fuel. *J. Am. Chem. Soc.* **2010**, *132*, 14385–14387.
83. Zhou, Y.; Tian, Z.; Zhao, Z.; Liu, Q.; Kou, J.; Chen, X.; Gao, J.; Yan, S.; Zou, Z. High-Yield Synthesis of Ultrathin and Uniform Bi₂WO₆ Square Nanoplates Benefitting from Photocatalytic Reduction of CO₂ into Renewable Hydrocarbon Fuel under Visible Light. *ACS Appl. Mater. Interfaces* **2011**, *3*, 3594–3601.
84. Li, X.; Pan, H.; Li, W.; Zhuang, Z. Photocatalytic Reduction of CO₂ to Methane over HNb₃O₈ Nanobelts. *Appl. Catal., A* **2012**, *413/414*, 103–108.
85. Lekse, J. W.; Underwood, M. K.; Lewis, J. P.; Matranga, C. C. Synthesis, Characterization, Electronic Structure, and Photocatalytic Behavior of CuGaO₂ and CuGa_{1-x}Fe_xO₂ ($x = 0.05, 0.10, 0.15, 0.20$) Delafossites. *J. Phys. Chem. C* **2012**, *116*, 1865–1872.
86. Iizuka, K.; Wato, T.; Miseki, Y.; Saito, K.; Kudo, A. Photocatalytic Reduction of Carbon Dioxide over Ag Cocatalyst-Loaded ALa₄Ti₄O₁₅ (A = Ca, Sr, and Ba) Using Water as a Reducing Reagent. *J. Am. Chem. Soc.* **2011**, *133*, 20863–20868.
87. Kohno, Y.; Tanaka, T.; Funabiki, T.; Yoshida, S. Photoreduction of Carbon Dioxide with Hydrogen over ZrO₂. *Chem. Commun.* **1997**, 841–842.
88. Aurian-Biajani, B.; Halmann, M.; Manassen, J. Electrochemical Measurement on the Photoelectrochemical Reduction of Aqueous Carbon Dioxide on p-Gallium Phosphide and p-Gallium Arsenide Semiconductor Electrodes. *Solar Energy Mater.* **1983**, *8*, 425–440.
89. Canfield, D.; Frese, K. W., Jr Reduction of Carbon Dioxide to Methanol on n- and p-GaAs and p-InP. Effect of Crystal Face, Electrolyte and Current Density. *J. Electrochem. Soc.* **1983**, *130*, 1772–1773.
90. Izumi, Y.; Itoi, T.; Peng, S.; Oka, K.; Shibata, Y. Site Structure and Photocatalytic Role of Sulfur or Nitrogen-Doped Titanium Oxide with Uniform Mesopores under Visible Light. *J. Phys. Chem. C* **2009**, *113*, 6706–6718.